

# PCCCP

Physical Chemistry Chemical Physics

Accepted Manuscript

This article can be cited before page numbers have been issued, to do this please use: S. A. Tatulian, *Phys. Chem. Chem. Phys.*, 2024, DOI: 10.1039/D4CP01136H.



This is an Accepted Manuscript, which has been through the Royal Society of Chemistry peer review process and has been accepted for publication.

Accepted Manuscripts are published online shortly after acceptance, before technical editing, formatting and proof reading. Using this free service, authors can make their results available to the community, in citable form, before we publish the edited article. We will replace this Accepted Manuscript with the edited and formatted Advance Article as soon as it is available.

You can find more information about Accepted Manuscripts in the [Information for Authors](#).

Please note that technical editing may introduce minor changes to the text and/or graphics, which may alter content. The journal's standard [Terms & Conditions](#) and the [Ethical guidelines](#) still apply. In no event shall the Royal Society of Chemistry be held responsible for any errors or omissions in this Accepted Manuscript or any consequences arising from the use of any information it contains.

# Analysis of Protein-Protein and Protein-Membrane Interactions by Isotope-Edited Infrared Spectroscopy

Suren A. Tatulian

Department of Physics, University of Central Florida, Orlando, FL

## AUTHOR INFORMATION

Corresponding Author

Suren A. Tatulian – Department of Physics, University of Central Florida, Orlando, Florida 32816, USA; orcid.org/0000-0002-5650-6946; Email: statulia@ucf.edu

**KEYWORDS:** isotope-edited infrared spectroscopy, protein structure, protein-membrane interaction, protein engineering

**ABBREVIATIONS:** aaRS, amino acyl tRNA synthetase; A $\beta$ , amyloid  $\beta$ ; AD, Alzheimer's disease; AFM, atomic force microscopy; ATR, attenuated total reflection; FTIR, Fourier transform infrared; DPPC, dipalmitoylphosphatidylcholine; DPPG, dipalmitoylphosphatidylglycerol; HO, harmonic oscillator; HX, hydrogen-deuterium exchange; IBS, interfacial binding site; IR, infrared; IRE, internal reflection element; PLA<sub>2</sub>, phospholipase A<sub>2</sub>; PLB, phospholamban; SR, sarcoplasmic reticulum.



**ABSTRACT:** The objective of this work is to highlight the power of isotope-edited Fourier transform infrared (FTIR) spectroscopy in resolving important problems encountered in biochemistry, biophysics, and biomedical research, focusing on protein-protein and protein membrane interactions that play key roles in practically all life processes. An overview of the effects of isotope substitutions in (bio)molecules on spectral frequencies and intensities is given. Data are presented demonstrating how isotope-labeled proteins and/or lipids can be used to elucidate enzymatic mechanisms, the mode of membrane binding of peripheral proteins, regulation of membrane protein function, protein aggregation, and local and global structural changes in proteins during functional transitions. The use of polarized attenuated total reflection FTIR spectroscopy to identify the spatial orientation and the secondary structure of a membrane-bound interfacial enzyme and the mode of lipid hydrolysis is described. Methods of production of site-directed, segmental, and domain-specific labeling of proteins by the synthetic, semisynthetic, and recombinant strategies, including advanced protein engineering technologies such as nonsense suppression and frameshift quadruplet codons are overviewed.

## 1. INTRODUCTION

Protein-protein interactions play a crucial role in nearly all aspects of cell physiology, such as cell signaling, reception, immunology, metabolism, muscle contraction, cell adhesion etc.<sup>1-3</sup> Moreover, defects in protein-protein interactions constitute the core cause of many diseases.<sup>4-6</sup> On the other hand, interactions of proteins with cellular membranes are central to many vital processes such as transport and homeostasis of ions and molecules, endo- and exocytosis, interfacial enzymology, etc.<sup>7-9</sup> Therefore, development of capable methods of analysis and characterization of such interactions is of pivotal importance for understanding the intricate molecular machinery driving life processes. Apart from the atomic- or near-atomic-resolution structural techniques like X-ray crystallography, nuclear magnetic resonance, cryo-electron microscopy and tomography,<sup>10-12</sup> single molecule imaging,<sup>13,14</sup> and advanced versions of atomic force microscopy,<sup>13-16</sup> other methods that are conventionally considered low-resolution comprise incompletely appreciated structure-resolving power. One of such techniques is Fourier transform infrared (FTIR) spectroscopy, including its various versions such as polarized attenuated total reflection (ATR) and isotope-edited FTIR.

FTIR is vibrational spectroscopy that can be described with rather high fidelity using the harmonic oscillator (HO) approach (see the next section), according to which the vibrational frequency ( $\nu$ ) of a diatomic molecule of atomic masses of  $m_1$  and  $m_2$  is:<sup>17</sup>

$$\nu = \frac{1}{2\pi} \sqrt{\frac{k}{\mu}} = \frac{1}{2\pi} \sqrt{k \left( \frac{1}{m_1} + \frac{1}{m_2} \right)} \quad (1)$$

In Eq. 1,  $\mu$  is the reduced mass of the two atoms:  $\mu = m_1 m_2 / (m_1 + m_2)$ . According to Eq. 1,  $\nu$  is sensitive not only to the types of the two atoms with specific atomic masses, such as C and O, but also to the strength of the covalent bond between them ( $k$ ), such as a single or a double bond. Moreover, hydrogen bonding (H-bonding) of the oxygen weakens the C=O covalent bond and thereby reduces the vibrational frequency, allowing identification of the presence and the strength of H-bonding that stabilizes protein structure. Furthermore, replacement of one or both atoms with a heavier isotope will generate a downshifted vibrational frequency, permitting analysis of a protein's local structure and dynamics, as described in the forthcoming sections.



The multiple vibrational modes of the amide group of proteins, i.e., amide I through amide VII as well as the amide A and B modes, generate absorbance bands at specific mid-infrared frequencies that are sensitive to the protein's secondary and tertiary structure.<sup>18</sup> The amide I mode (1700–1600 cm<sup>-1</sup>) is mostly due to the C=O stretching vibration, with small contributions from the C–N, C–C–N, and N–H vibrations. Its frequency depends on the local geometry of the protein backbone and interactions between chemical groups such as H-bonding between the main-chain C=O and N–H groups and through scape vibrational coupling effects. Hence, the amide I band is exquisitely sensitive to the protein secondary structure. Due to the spectral overlap between the H<sub>2</sub>O bending mode and the protein amide I mode, a D<sub>2</sub>O-based buffer is usually used in FTIR experiments. The use of D<sub>2</sub>O results in a slight red shift of amide I frequencies caused by amide hydrogen/deuterium exchange (HX). The main secondary structures of a protein, such as various  $\beta$ - and  $\gamma$ -turns,  $\alpha$ -helix,  $\beta$ -sheet, irregular structure, can be pinpointed based on their characteristic amide I wavenumbers ( $\tilde{\nu} = 1/\lambda = \nu/c$ , where  $\lambda$  is the wavelength and  $c$  is the speed of light). The approximate wavenumber ranges for proteins in H<sub>2</sub>O (and D<sub>2</sub>O, shown in parentheses) are as follows: 1700–1660 cm<sup>-1</sup> (1690–1650 cm<sup>-1</sup>) for  $\gamma$ -turns, 1685–1655 cm<sup>-1</sup> (1675–1640 cm<sup>-1</sup>) for  $\beta$ -turns, 1660–1648 cm<sup>-1</sup> (1655–1638 cm<sup>-1</sup>) for  $\alpha$ -helix, 1660–1652 cm<sup>-1</sup> (1648–1640 cm<sup>-1</sup>) for irregular structure, and 1638–1630 cm<sup>-1</sup> (1635–1625 cm<sup>-1</sup>) for  $\beta$ -sheet. Moreover, various subtypes of same secondary structure can be distinguished. For example, the  $\alpha_{II}$ -helix, which has identical geometric parameters with the regular  $\alpha$ -helix (rise per amino acid along the helical axis, number of amino acids per turn) but slightly tilted amide plane and hence weaker C=O...H–N H-bonding and stronger C=O and H–N covalent bonds, generates amide I signal at higher wavenumbers,  $\sim$ 1665 cm<sup>-1</sup>, making FTIR a unique tool for detection of this structure. FTIR is also uniquely suited to distinguish between parallel and antiparallel and between intramolecular and intermolecular  $\beta$ -sheets as antiparallel  $\beta$ -sheets generate an additional (albeit weak) component at higher wavenumbers (around 1680 cm<sup>-1</sup>) and the wavenumbers of intermolecular  $\beta$ -sheets, e.g. in aggregated proteins or amyloid peptides, are shifted towards lower wavenumbers (1625–1615 cm<sup>-1</sup>).<sup>18</sup>

The amide II mode occurs around 1550 cm<sup>-1</sup> in H<sub>2</sub>O and is mostly due to the amide N–H in-plane bending mode. In D<sub>2</sub>O, the amide hydrogens undergo exchange with deuterium of the solvent, if exposed and not involved in strong intramolecular H-bonding, resulting in a  $\sim$ 90 cm<sup>-1</sup> downshift of the amide II mode. Thus, the extent and the kinetics of the amide HX, i.e. the rate of reduction of the  $\sim$ 1550 cm<sup>-1</sup> signal, is diagnostic for the extent of solvent exposure (tertiary structure) and the degree of involvement in H-bonding (secondary structure). Other amide modes are less sensitive to protein structure or dynamics, yet have been used for protein structural studies, as described in more detail elsewhere.<sup>18</sup>

The ATR-FTIR spectroscopy is a surface-sensitive version of FTIR that is based on creation of an evanescent field at the surface of an infrared-transparent internal reflection element (IRE), such as a germanium plate, during internal reflection of the infrared light within the IRE. As the evanescent wave decays with a characteristic length of 300–400 nm, this technique detects the sample, such as a lipid membrane with reconstituted protein(s) deposited on the surface of the IRE. Plane-polarized infrared light is usually used to study not only the structural features of membrane proteins and lipids but also their spatial orientation.

The isotope-edited FTIR, which is the main topic of this article, is based on the spectral shift of the infrared signal due to replacement of atoms in biomolecules, such as H, C, N, by nonradioactive isotopes, such as <sup>2</sup>H (D), <sup>13</sup>C, <sup>15</sup>N. For example, a lipid molecule with one unlabeled and one deuterated acyl chain generates infrared signals separated by  $\sim$ 730 cm<sup>-1</sup>,



which allows identification of selective cleavage of the *sn*-1 and *sn*-2 chains by phospholipase A<sub>2</sub> (PLA<sub>2</sub>), reflecting the enzyme's mechanism.<sup>19</sup> Combination of a <sup>13</sup>C-labeled protein with an unlabeled protein results in amide I band splitting, allowing analysis of dynamic structural changes in each protein during intermolecular interactions.<sup>20</sup> Site directed or segmental <sup>13</sup>C (or <sup>13</sup>C, <sup>15</sup>N or <sup>13</sup>C=<sup>18</sup>O) labeling of a protein allows determination of the local conformational dynamics during functional transitions.<sup>21-23</sup> The production of isotope-labeled proteins ranges from easy (e.g., uniform labeling by expression in bacteria grown a minimal medium containing a sole labeled nutrient) to moderate difficulty (e.g., chemical ligation of an unlabeled fragment of a protein with a labeled peptide or incorporation of a single labeled amino acid by the nonsense suppression method).

Apart from the advanced capabilities of FTIR spectroscopy, other features such as the relative simplicity of the experimental setup, the ease of the measurements and data analysis, the small amount of material per experiment (typically, around 50 μg of protein or lipid), and the wealth of the information on the structure of both protein and lipid (if present) from just one spectrum measured in 5 minutes, make the method attractive for broad applications, e.g. protein-protein and protein-lipid interactions and beyond.

## 2. ISOTOPE EFFECTS ON ABSORBANCE FREQUENCY AND INTENSITY

### 2.1. Model Compounds

Replacement of an atom in a chemical group —X—Y by an isotope of different nuclear mass will shift the X—Y vibrational frequency. If Y has a much smaller mass than X, the X—Y stretching vibration can be considered as harmonic oscillation since Y will be essentially involved in the oscillation (like a ping pong ball attached to a bowling ball by a spring) and the frequency will be determined mainly by its mass ( $\mu \approx m_Y$ ). Then, the frequency shift resulting from replacement of Y by an isotope (e.g., replacement of C—H with C—D or N—H with N—D) can be predicted using Eq. 1. If the mass of Y is not very small, the HO approach is still valid when the X—Y bond is much stronger than the other bonds in a polyatomic molecule, such as the C=O double bond.<sup>17</sup> Thus, the C—H to C—D, N—H to N—D, and <sup>12</sup>C=<sup>16</sup>O to <sup>13</sup>C=<sup>16</sup>O or to <sup>13</sup>C=<sup>18</sup>O isotopic replacements, often used in protein and lipid FTIR spectroscopy, are expected to obey the HO rules, in particular the Eq. 1, with acceptable accuracy.

The HO theory predicts that the C—H to C—D isotopic change will decrease the vibrational frequency by a factor of  $\nu^i/\nu = 0.7338$  ( $\nu^i$  and  $\nu$  are the frequencies of the heavier isotopic and normal forms, respectively). This prediction is valid so long as the molecule is free from any kind of intermolecular interactions, ideally, when it is in gas phase.<sup>17</sup> Vibrational coupling effects or interactions with the solvent or other solute molecules, e.g. via H-bonding, may drastically affect the resulting frequencies and intensities (see below). For example, the methylene asymmetric stretching wavenumbers of the CH<sub>4</sub> and CD<sub>4</sub> isotopomers of methane were 3019 cm<sup>-1</sup> and 2259 cm<sup>-1</sup>, respectively.<sup>17</sup> This corresponds to a factor of 0.7483, which agrees with the HO prediction with 2% accuracy. The respective wavenumber of <sup>13</sup>CH<sub>4</sub> was 3010 cm<sup>-1</sup>, as expected for a diatomic HO. The <sup>13</sup>C=O stretching vibration of 3-<sup>13</sup>C-2,4-dimethyl-3-pentanone, 1-<sup>13</sup>C-2-methylpropionoc acid, and C<sub>6</sub>H<sub>5</sub><sup>13</sup>COOH (benzoic acid) dissolved in organic solvents was downshifted by 35-37 cm<sup>-1</sup> as compared to the wavenumbers of their normal (unlabeled) counterparts, in good agreement with the HO theory.<sup>17</sup>



Linear hydrocarbons in condensed phase produced strong infrared peaks in spectral regions 2926-2915  $\text{cm}^{-1}$  and 2855-2845  $\text{cm}^{-1}$  attributed to the antisymmetric and symmetric methylene stretching vibrations, and the respective wavenumbers of their perdeuterated (i.e., totally deuterated) counterparts were red shifted by  $>700 \text{ cm}^{-1}$ .<sup>24,25</sup> For *n*-hexadecane, the spectral shifts were from 2926  $\text{cm}^{-1}$  to 2198  $\text{cm}^{-1}$  and from 2854  $\text{cm}^{-1}$  to 2095  $\text{cm}^{-1}$ .<sup>25</sup> These data indicate that the spectral shift of the symmetric stretching vibration agrees with the diatomic HO prediction ( $\nu^i/\nu = 0.7341$  as compared to the predicted value of 0.7338) but is less for the antisymmetric vibration ( $\nu^i/\nu = 0.7512$ ), resulting in a wider separation between the perdeuterated peaks. The symmetric mode has been shown to be affected by intra- and intermolecular Fermi resonance interactions with the methylene bending mode, which results in secondary bands that contribute to the apparent intensity increase in the antisymmetric stretching region.<sup>26</sup> Such interactions are symmetry-forbidden for the antisymmetric stretching mode of an extended chain.

For molecules in gas phase, the change in the integrated molar absorption intensity ( $A$ ) is predicted to be proportional to the square of the change in frequency:<sup>17</sup>

$$\frac{A^i}{A} = \left(\frac{\nu^i}{\nu}\right)^2 \quad (2)$$

where the superscript  $i$  means the isotopic form. Accordingly, the  $A^i/A$  ratio for  $\text{CD}_4$  and  $\text{CH}_4$  was 0.6260 as compared to  $(\nu^i/\nu)^2 = 0.5599$ , signifying a fairly good agreement with the theory.<sup>17</sup>

## 2.2. Peptides and Proteins

For proteins or lipid bilayers, which are in the condensed phase and are involved in a multitude of trough-space and trough-bond intermolecular interactions, the HO predictions are not expected to strictly hold. In addition, the spectral shifts of the amide I signal due to the most frequently utilized  $^{13}\text{C}=\text{O}$  labeling strategy cannot be described by a simple diatomic HO modeling as the amide I mode is not a pure  $\text{C}=\text{O}$  stretching vibration. Nonetheless, incorporation of just one or up to 5 consecutive backbone  $^{13}\text{C}=\text{O}$ -labeled amino acid residues in synthetic peptides produced a new amide I peak red shifted from that of the unsubstituted peptide by  $37 \pm 4 \text{ cm}^{-1}$ , in agreement with the HO theory applied to an isolated  $\text{C}=\text{O}$  bond.<sup>27-34</sup> Incorporation of  $^{13}\text{C}$ -labeled amino acids located consecutively or separated by one or more  $^{12}\text{C}$  units in a  $\alpha$ -helical 25-mer peptide revealed a complex behavior of both the vibrational frequency and intensity.<sup>33,34</sup> The frequency of a single  $^{13}\text{C}$  amide unit was downshifted by  $36\text{-}37 \text{ cm}^{-1}$  (from  $1632\text{-}1630 \text{ cm}^{-1}$  to  $1596\text{-}1593 \text{ cm}^{-1}$ ) and increasing number of  $^{13}\text{C}$  units resulted in increase in both  $^{12}\text{C}$  and  $^{13}\text{C}$  frequencies, increase in  $^{13}\text{C}$  intensity, and decrease in  $^{12}\text{C}$  intensity<sup>34</sup>. Variably spaced  $^{13}\text{C}$  units produced a non-monotonous (“damped sinusoidal”) dependence of the downshifted frequency on the number of intervening  $^{12}\text{C}$  units. Strikingly, the presence of one or two  $^{12}\text{C}$  units between two  $^{13}\text{C}$  units produced amide I signal of reduced intensity downshifted by additional  $\sim 10 \text{ cm}^{-1}$ .<sup>33,34</sup> These effects were interpreted in terms of distinct distance dependencies of the through-covalent-bonding mechanical coupling and through-space electrostatic and transition dipole couplings as well as relative dipolar orientations of the amide oscillators at defined positions along the spiraling helical chain.<sup>21,34</sup> The increased frequency and



reduced intensity of the  $^{12}\text{C}$  signal upon incorporation of more  $^{13}\text{C}$  units is thought to be caused by vibrational decoupling between the  $^{12}\text{C}$  amide oscillators.<sup>34</sup>

The amide I intensity depends on the secondary structure and its continuity and is different for  $^{12}\text{C}=\text{O}$  and  $^{13}\text{C}=\text{O}$  peptide segments. For example, the molar absorption coefficient at the maximum of the amide I band ( $\epsilon_{\text{max}}$ ) was  $640 \text{ M}^{-1}\text{cm}^{-1}$  at  $1^\circ\text{C}$  (mostly helical structure) and  $392 \text{ M}^{-1}\text{cm}^{-1}$  at  $91^\circ\text{C}$  (mostly unordered) for the unlabeled ( $^{12}\text{C}=\text{O}$ ) peptide<sup>30</sup> (here,  $\text{M}^{-1}$  means per M of amino acid units, not per M of). The respective values of  $\epsilon_{\text{max}}$  were smaller for the  $^{13}\text{C}$ -labeled segments by a factor of 0.7-0.8. This difference in molar absorptivity was explained by higher helicity and longer chains of the unlabeled segments rather than by intrinsic, isotope-specific differences<sup>30</sup> echoing with the concept of disruption of the  $^{12}\text{C}=\text{O}/^{12}\text{C}=\text{O}$  coupling by intervening  $^{13}\text{C}=\text{O}$  units mentioned above.<sup>34</sup> This is reminiscent of the up to 2-fold stronger amide I signal from the  $^{13}\text{C}$ -labeled 4-residue segment located centrally compared to that when located at the N- or C-termini of a 20-mer helical peptide.<sup>28,35</sup>

The agreement between the observed and diatomic HO-predicted frequency shift of  $\sim 37 \text{ cm}^{-1}$  upon a  $>^{12}\text{C}=\text{O} \rightarrow >^{13}\text{C}=\text{O}$  substitution may be fortuitous due to compensation of diverse effects on the resulting vibrational frequency. When other amide I components such as the C—N stretching mode are included in the computation, the  $^{13}\text{C}$ -induced spectral shift is around  $43 \text{ cm}^{-1}$  rather than  $37 \text{ cm}^{-1}$ .<sup>36</sup> Uniform  $^{13}\text{C}$ -labeling of 40-42 amino acid residue peptides reduced the amide I frequency from  $1658 \text{ cm}^{-1}$  to  $1617 \text{ cm}^{-1}$  in  $\alpha$ -helical state and from  $1633 \text{ cm}^{-1}$  to  $1590 \text{ cm}^{-1}$  in  $\beta$ -sheet state, i.e. a  $41\text{-}43 \text{ cm}^{-1}$  downshift as predicted by the more accurate simulation.<sup>37</sup> Likewise, other studies on chemically synthesized or recombinantly produced proteins reported  $40\text{-}44 \text{ cm}^{-1}$  downshift of the amide I peak due to singly, segmentally, or uniform  $^{13}\text{C}=\text{O}$  labeling,<sup>38-41</sup> while the spectral shift due to uniform  $^{13}\text{C}$ ,  $^{15}\text{N}$  labeling of recombinant proteins was  $45\text{-}55 \text{ cm}^{-1}$ .<sup>42,43</sup>

Apart from intramolecular vibrational couplings, the amide I frequency also depends on H-bonding with the solvent. Thus, for totally hydrated  $\alpha$ -helical peptides that form H-bonding with water, the frequency is reduced by as much as  $17 \text{ cm}^{-1}$ , e.g., from  $\sim 1650 \text{ cm}^{-1}$  down to  $\sim 1633 \text{ cm}^{-1}$ .<sup>21</sup> Peptides in dry state (dried from hexafluoroisopropanol solution)<sup>37,44</sup> or embedded in lipid bilayers<sup>40,45</sup> show amide I peaks around  $1661\text{-}1657 \text{ cm}^{-1}$  as compared to  $1633 \pm 4 \text{ cm}^{-1}$  displayed by peptides totally hydrated in a  $\text{D}_2\text{O}$  buffer.<sup>28,30,33,34</sup> A similar effect has been reported for a  $\beta$ -sheet peptide.<sup>46</sup>

Studies on peptides in  $\beta$ -sheet conformation revealed position-dependent  $^{13}\text{C}$  isotopic shifts in spectral frequencies and absorbance intensities.<sup>29,46-49</sup> Incorporation of one or two  $^{13}\text{C}=\text{O}$  amino acids in a synthetic, antiparallel  $\beta$ -sheet forming tetradecapeptide produced a spectrally downshifted (from  $1634\text{-}1628 \text{ cm}^{-1}$  to  $1611\text{-}1606 \text{ cm}^{-1}$ ) amide I component of anomalously high intensity.<sup>29</sup> The integrated molar absorptivity of the downshifted amide I component of a single  $^{13}\text{C}=\text{O}$  label was more than doubled relative to that of the main  $^{12}\text{C}=\text{O}$  part, i.e. constituted around 17% of the total amide I contour as opposed to the expected  $1/14 \approx 7\%$ . The peptide with two consecutive labels generated a similar amide I band. However, when the two  $^{13}\text{C}=\text{O}$  labels were separated by one  $^{12}\text{C}=\text{O}$  unit, the absorptivity increased nearly 2-fold compared to the species with two consecutive  $^{13}\text{C}=\text{O}$  labels. These anomalous intensities were interpreted by through-space transition dipole coupling and through covalent bonding and through H-bonding interactions between the  $^{13}\text{C}=\text{O}$  and  $^{12}\text{C}=\text{O}$  amide oscillators. In case of single or sequential double labeled peptides, the  $^{13}\text{C}$ -substituted oscillators borrow intensity from the unlabeled oscillators of both opposite (through H-bonding) and same (through covalent bonding) strands whereas the separated oscillators do the same but pick up more intensity from



neighboring  $^{12}\text{C}=\text{O}$  units through covalent bonding. Interestingly, in case of an  $\alpha$ -helical peptide, a single  $^{13}\text{C}=\text{O}$  substitution produced an amide I component downshifted by  $\sim 38\text{ cm}^{-1}$  as expected for an isolated oscillator, suggesting the absence of (or weaker) through-H-bond interactions in  $\alpha$ -helix compared to  $\beta$ -sheet, consistent with a shorter  $\text{N}\cdots\text{O}$  distance by  $0.034\text{ \AA}$  in the latter case.<sup>29</sup> In addition to this difference, Huang et al.<sup>33</sup> reported that in  $\alpha$ -helical structure the isotopically substituted groups are coupled essentially to each other but not to the unlabeled units, in contrast to  $\beta$ -sheet structure.

An important feature observed in  $\beta$ -sheet peptides, which has helped distinguish between parallel and antiparallel  $\beta$ -sheets, is that the spectral downshift of the  $^{13}\text{C}=\text{O}$  substituted units that are involved in coupling with each other is larger by  $\sim 10\text{ cm}^{-1}$  compared to that caused by  $^{13}\text{C}=\text{O}/^{12}\text{C}=\text{O}$  coupling ( $1594\text{--}1591\text{ cm}^{-1}$  and  $1604\text{--}1601\text{ cm}^{-1}$ , respectively).<sup>46,47,50,51</sup> The effects of vibrational couplings between same or different isotope units on vibrational frequencies and intensities has been demonstrated in studies on a dodecamer that forms a  $\beta$ -hairpin structure with amide I peak at  $1633\text{ cm}^{-1}$ .<sup>48</sup> Incorporation of two  $^{13}\text{C}=\text{O}$  units in opposing strands produced a new component that was downshifted more when the labeled  $^{13}\text{C}=\text{O}$  oscillators were spatially (not along the chain) closer. In addition, the more downshifted signal (closer spacing) was less intense than the less downshifted signal generated by more remotely spaced units. These features were interpreted by  $^{13}\text{C}=\text{O}/^{13}\text{C}=\text{O}$  and  $^{12}\text{C}=\text{O}/^{13}\text{C}=\text{O}$  vibrational coupling effects: closely spaced  $^{13}\text{C}=\text{O}$  oscillators couple stronger resulting in a larger downshift but do not mix with the  $^{12}\text{C}=\text{O}$  modes whereas those spaced more distantly (more  $^{12}\text{C}=\text{O}$  units in between) experience less  $^{13}\text{C}=\text{O}/^{13}\text{C}=\text{O}$  coupled (higher frequency) and more  $^{12}\text{C}=\text{O}/^{13}\text{C}=\text{O}$  coupling (higher intensity through mixing). These data underscore the dependence of spectral frequencies and intensities caused by  $^{13}\text{C}$ -labeling on the number and location of labeled residues. Upon insertion of 3 backbone  $^{13}\text{C}=\text{O}$  units in a 3-stranded antiparallel  $\beta$ -sheet peptide (one per strand), the  $^{12}\text{C}=\text{O}$  frequency of the main  $\beta$ -sheet rose to  $1642\text{ cm}^{-1}$ , resulting in a  $54\text{ cm}^{-1}$  spectral gap between labeled and unlabeled signals.<sup>49</sup> This effect is explained by reduction of the strand length and subsequent disruption of coupling between  $^{12}\text{C}=\text{O}$  oscillators,<sup>49</sup> like in case of  $\alpha$ -helix discussed above.<sup>34</sup>

Double isotopic labeling of the amide carbonyl with  $^{13}\text{C}$  and  $^{18}\text{O}$  provides a better resolution of the local structure of proteins or peptides.<sup>40</sup> Labeling one out of 25 residues of an  $\alpha$ -helical peptide with  $^{13}\text{C}=\text{O}^{18}\text{O}$  resulted in an amide I component shifted to  $1595\text{ cm}^{-1}$  from the main (unlabeled) component centered at  $1659\text{ cm}^{-1}$ .<sup>40</sup> This  $64\text{ cm}^{-1}$  shift is less than the  $78\text{ cm}^{-1}$  predicted by diatomic HO calculations but is consistent with a more rigorous Hartree-Fock theory. The robust spectral resolution permitted determination of the local structure and orientation of the transmembrane domains of membrane proteins by ATR-<sup>52,53</sup> or transmission FTIR<sup>54</sup> on oriented peptide/lipid films. 2D infrared studies on another helical peptide  $^{13}\text{C}=\text{O}^{18}\text{O}$  labeled at 1 position at a time spanning the central 11 residues, mixed with the unlabeled peptide at various proportions in lipid vesicles, revealed excitonic through-space vibrational coupling (delocalization) between the labeled oscillators, or the absence of such coupling at higher dilutions, which allowed construction of the structure of the transmembrane helical dimer.<sup>55</sup>

For peptides forming cross- $\beta$ -sheet amyloid fibrils, such as the amyloid  $\beta(1\text{--}40)$  peptide, a main amide I peak was detected at  $1625\text{ cm}^{-1}$  and a downshifted component in the  $1585\text{--}1575\text{ cm}^{-1}$  range depending on the position of the  $^{13}\text{C}=\text{O}^{18}\text{O}$  substituted residue.<sup>56</sup> The spectral shift was stronger for the sample composed of the labeled peptide due to vibrational coupling along the fibril axis and was blue shifted by  $\sim 20\text{ cm}^{-1}$  (from  $\sim 1575\text{ cm}^{-1}$  to  $\sim 1595\text{ cm}^{-1}$ ) when combined with a large molar excess of the unlabeled peptide. In contrast to  $\alpha$ -helix, where a single label





may not produce a diagnostic signal because of the absence of coupling with another labeled residue, the isotopic substitution of a single amino acid in parallel in-register fibril forming peptides produces a strongly delocalized and red shifted normal mode indicative of interstrand coupling along the fibril axis.<sup>57,58</sup> A heptadecapeptide with  $^{13}\text{C}=\text{O}$  substituted alanine at position 5 or 15 displayed amide I spectra with a major peak at 1632 or 1629  $\text{cm}^{-1}$  and a minor (isotope-induced) peak at 1587 or 1591  $\text{cm}^{-1}$ , signifying a 45  $\text{cm}^{-1}$  or 38  $\text{cm}^{-1}$  red shift for the N- and C-terminal segments that were deduced to be in ordered cross- $\beta$  and unordered conformations, respectively.<sup>59</sup> Thus, the  $^{13}\text{C}=\text{O}$  isotope-induced frequency shift in  $\beta$ -sheet peptides was significantly less ( $\sim 45\text{--}50\text{ cm}^{-1}$ )<sup>56,59</sup> than that in  $\alpha$ -helices ( $\sim 65\text{ cm}^{-1}$ ).<sup>40,52-54</sup>

The human islet amyloid polypeptide in both  $\alpha$ -helical and  $\beta$ -sheet conformations, incorporating 1 or 2 adjacent  $^{13}\text{C}=\text{O}$  labeled residues, was studied by 2D infrared spectroscopy.<sup>58</sup> Incorporation of a single label into the  $\alpha$ -helical or  $\beta$ -sheet structure caused a  $\sim 55\text{ cm}^{-1}$  and  $32\text{--}42\text{ cm}^{-1}$  red shift, respectively, in qualitative agreement with the above assessment. The respective red shifts caused by two adjacent labels were  $\sim 45\text{ cm}^{-1}$  and  $\sim 52\text{ cm}^{-1}$  however, reversing the disparity between  $\alpha$ -helical and  $\beta$ -sheet structures. This effect was consistent with normal mode analysis which highlighted differences between spectral shifts due to single vs. double (adjacent) labels in the two structures: two adjacent isotope labels cause a red shift from the uncoupled local mode frequency of the isotope substituted group for a  $\beta$ -sheet structure (through intra- and interstrand couplings) and a blue shift for  $\alpha$ -helix (through covalent bond coupling).<sup>58</sup>

The above discussions underscore the complexity of the behavior of vibrational frequencies and intensities and the involved isotopic effects. The frequencies and intensities of labeled vibrations depend on the secondary structure, the number of the labels and their sequentiality. The isotope labeling strategy should be selected taking into account the targeted secondary structure. For example, spectral features of a single isotope in an  $\alpha$ -helix will produce only a local mode bearing little structural information but in a parallel in-register  $\beta$ -sheet structure or a cross- $\beta$ -sheet structure a single label will be strongly coupled along and across the sheet plane producing the diagnostic amide I signal.<sup>49,58</sup>

Interpretation of the shifted frequency in terms of secondary structure is not straightforward. For example, the  $\sim 1633\text{ cm}^{-1}$  signal can be generated by  $\beta$ -sheet<sup>48,49</sup> or by hydrated and totally amide deuterated  $\alpha$ -helix.<sup>21,30-32,34</sup> Additional methods such as circular dichroism or NMR are required to identify whether the spectral shift, e.g. from  $\sim 1655\text{ cm}^{-1}$  to  $\sim 1635\text{ cm}^{-1}$ , reflects an  $\alpha \rightarrow \beta$  transition of hydration of the protein's backbone carbonyls plus amide HX.<sup>29,30,49</sup> The amide I signal in the spectrum of a  $^{13}\text{C}=\text{O}$  or  $^{13}\text{C}=\text{O}$  labeled peptide or protein in the  $1600\text{--}1565\text{ cm}^{-1}$  region should be treated cautiously as it may be produced by either the labeled amino acid or the side chains of certain amino acids such as arginine or glutamic acid.<sup>30,48,56</sup> Finally, possible artifacts stemming from the admixture of  $^{13}\text{C}$  due to natural abundance ( $\sim 1.1\%$ ) should be kept in mind to avoid misinterpretation of the intensity of the signal generated by the labeled site.

### 2.3. Lipids

Artificial membranes composed of isotopically labeled lipids have been used to study thermal phase transitions, lateral segregation, lipid transfer, lipid-protein interactions, and the influence thereof on the function of membrane proteins.<sup>60-64</sup> Mostly, the acyl chain deuterated or carbonyl



$^{13}\text{C}=\text{O}$  substituted lipids have been used to gain structural information on the membrane core or the polar headgroup region. The acyl chain methylene groups generate antisymmetric and symmetric stretching vibrations centered around  $2920\text{ cm}^{-1}$  and  $2850\text{ cm}^{-1}$  in protiated ( $\text{CH}_2$ ) form while chain perdeuteration shifts these wavenumbers down to  $\sim 2192\text{ cm}^{-1}$  and  $\sim 2090\text{ cm}^{-1}$ , respectively.<sup>25,60,65,66</sup> The methylene stretching modes of perdeuterated chains are usually less intense in terms of peak height and the spectral spacing between the symmetric and antisymmetric peaks is larger ( $\sim 100\text{ cm}^{-1}$ ) compared to the unlabeled lipids ( $\sim 70\text{ cm}^{-1}$ ), similar to the features detected for *n*-alkanes discussed above. Analysis of ATR-FTIR spectra of unlabeled and acyl chain perdeuterated phospholipids produced nearly equal integrated molar absorption intensities:  $A^i/A \approx 1.0$ , indicating no isotope-induced changes in intrinsic absorptivities.<sup>60</sup>

Temperature-induced gel to liquid crystal phase transitions of bilayer membranes composed of unlabeled and acyl chain perdeuterated lipids cause increase in the stretching wavenumbers by  $2\text{--}5\text{ cm}^{-1}$ .<sup>63,65–68</sup> This spectral shift is interpreted in terms of decreased vibrational interactions between adjacent methylene units due to increasing ratio of gauche/trans conformational isomers.<sup>62,65,67</sup> Similar methylene stretching vibrational shifts have been detected upon isotopic dilution of *n*-alkanes as well as phospholipids without involvement of conformational changes, explained by alterations in intermolecular Fermi resonance between like isotopic species.<sup>25</sup> Use of lipids with perdeuterated acyl chains has permitted analysis of thermal phase transitions of individual membrane components composed of binary or ternary lipid mixtures.<sup>62,68,69</sup> Other vibrational modes of lipids such as the methylene rocking and scissoring modes and their spectral shifts upon deuteration have been analyzed to revealed membrane depth-dependent fractions of gauche rotamers and to detect lipid microdomain formation.<sup>70,71</sup>

The carbonyl stretching mode of glycerophospholipids in aqueous suspensions generates a band with a peak wavenumber in the  $1740\text{--}1730\text{ cm}^{-1}$  region which, upon resolution enhancement, reveals two components around  $1742\text{ cm}^{-1}$  and  $1727\text{ cm}^{-1}$ .<sup>67,72,73</sup> These two components have been assigned to the carbonyls at *sn*-1 and *sn*-2 ester groups, respectively, and the splitting was ascribed to their distinct conformations.<sup>67</sup> Further studies on lipids selectively  $^{13}\text{C}=\text{O}$  labeled at either *sn*-1 or *sn*-2 carbonyls resulted in two bands, the one generated by the labeled carbonyl red shifted by  $40\text{--}43\text{ cm}^{-1}$ .<sup>72–75</sup> Strikingly, both the unlabeled and the  $^{13}\text{C}=\text{O}$  labeled (and downshifted) bands were in turn composed of at least two components of their own separated by the same gap, i.e.  $11\text{--}17\text{ cm}^{-1}$ .<sup>72,74,75</sup> It was concluded that the higher and lower frequency components of the carbonyl stretching vibrations are generated by dehydrated and hydrated fractions of the carbonyl groups rather than structural difference that could account for a smaller ( $3\text{--}4\text{ cm}^{-1}$ ) spectral difference.<sup>72,74</sup> In general, an increasing polarity and H-bonding capability of the solvent results in lower frequency and wider vibrational bands.<sup>72,75</sup> The red shift upon hydration can be explained by weakening of the  $>\text{C}=\text{O}$  double bond (parameter *k* in Eq. 1) due to strong  $>\text{C}=\text{O}\cdots\text{H}-\text{O}-\text{H}$  hydrogen bonding.

FTIR studies on phosphatidylcholine selectively  $^{13}\text{C}=\text{O}$  labeled at one of the two ester carbonyls suggested that cholesterol forms H-bonding with the *sn*-2 but not *sn*-1 carbonyl group.<sup>76</sup> Polarized ATR-FTIR studies on substrate-supported multilayers of selectively  $^{13}\text{C}=\text{O}$  labeled phosphatidylcholines reported a  $\sim 40\text{ cm}^{-1}$  red shift of the  $\text{C}=\text{O}$  double bond and a  $\sim 20\text{ cm}^{-1}$  red shift of the ester  $\text{CO}-\text{O}$  single bond stretching vibrations, allowing determination of similar orientations of the  $\text{C}=\text{O}$  bonds of both chains ( $\geq 60^\circ$ ) and radically different orientations of the  $\text{CO}-\text{O}$  bonds relative to the membrane normal.<sup>73</sup>

Both the methylene and the carbonyl stretching modes of lipids have been used to assess protein-lipid interactions and activities of membrane proteins. FTIR data on acyl chain



perdeuterated phospholipids combined with unlabeled diacylglycerol identified domains of phosphatidylserine/diacylglycerol complexes that facilitated activation of protein kinase C.<sup>62</sup> Membrane binding of human 5-lipoxygenase caused a shift of the carbonyl stretching band to higher wavenumbers, suggesting membrane dehydration.<sup>77</sup> Fluorescence data on lipid vesicles containing a surface polarity-sensitive probe implied membrane dehydration upon PLA<sub>2</sub> binding, however the lower and higher frequency components of the lipid carbonyl stretching bands (1728 cm<sup>-1</sup> and 1742 cm<sup>-1</sup>) became stronger and weaker, respectively, indicating H-bonding between the protein and membrane lipids.<sup>78</sup> The mode of membrane binding and selective hydrolysis of membrane lipids by PLA<sub>2</sub> are described in detail in the forthcoming sections.

### 3. PROTEIN-MEMBRANE INTERACTIONS

#### 3.1. Hierarchy of Membrane Proteins and Modes of Interactions with Membranes

Around one-third of all gene products are membrane proteins,<sup>79,80</sup> clearly implying that protein-membrane interactions constitute one of the major pillars of the temple of life. These proteins employ distinct mechanisms of membrane binding. While the integral proteins possess well-defined nonpolar stretches that interact with membrane lipids via hydrophobic contacts, the lipid-tethered proteins utilize a covalently attached fatty acid (most frequently, palmitic or myristic), glycosylphosphatidylinositol, or isoprenoid (farnesyl or geranylgeranyl) moiety for membrane binding.<sup>81-91</sup> Polytopic proteins constitute the most abundant subclass of membrane proteins (>25%)<sup>8</sup> and may contain 2 to 16 transmembrane helices.<sup>81</sup> A smaller group of integral proteins utilizes an antiparallel transmembrane  $\beta$ -sheet structure arranged in a  $\beta$ -barrel-like architecture to serve as a transport passageway for relatively large molecules or as receptors, cell adhesion and/or signaling molecules in mitochondria of animal cells, chloroplasts of plant cells and plasma membranes of prokaryotes such as the bacterial toxin  $\alpha$ -hemolysin.<sup>8,82-84</sup>

The peripheral proteins have been estimated to constitute ~9% of the human proteome and perform their function through transient association with plasma or organellar membranes.<sup>7-9</sup> Some of these proteins are enzymes targeting membrane lipids for phosphorylation (e.g., diacylglycerol kinase, phosphatidylinositol 3-kinase), oxygenation (lipoxygenases), or hydrolysis (e.g., sphingomyelinase or phospholipases A<sub>1</sub>, A<sub>2</sub>, B, C, D). Typically, the peripheral proteins bind to membranes using an interfacial binding site (IBS).<sup>9</sup> As the IBS is not always a clearly defined motif or domain, identification of the mode of membrane interaction of peripheral proteins remains a challenge. Analysis of 1328 experimentally determined and 1194 simulated (AlphaFold) peripheral protein structures identified some common features of the IBS, i.e., protrusions rich in nonpolar amino acids (protruding hydrophobes)<sup>92</sup> and lysine, which support membrane binding through hydrophobic and ionic contacts, respectively.<sup>9</sup> In addition, there are many membrane binding modules specifically recognizing individual lipids or their assemblies. For example, most isoforms of protein kinase C become activated through binding to membrane-residing diacylglycerol using the C1 domain. Around 150 human proteins, including protein kinase C, contain one or more C2 domains, which mediate membrane binding, often in a calcium-dependent manner.<sup>93</sup> A range of signaling proteins bind to phosphatidylinositol phosphorylated at certain sites through the pleckstrin homology or FYVE domain, which recruit the respective proteins to distinct membranes where their function is most physiologically relevant.<sup>7</sup> Other specialized lipid binding domain families are described elsewhere.<sup>9,93</sup>



Peripheral proteins, including enzymes such as lipoxygenases, annexins, lipid kinases, phosphatases, and hydrolases, rely on binding to membranes with certain lipid composition, at a defined mode, including the depth of membrane insertion and the spatial orientation. The mode of membrane binding is crucial for the function of these proteins,<sup>94</sup> yet the “characterization of these fundamentally important lipid-protein interactions with experimental techniques is...prohibitively challenging”.<sup>95</sup> The forthcoming text will illustrate an example of how isotope-edited FTIR spectroscopy can determine the precise mode of membrane binding and thereby provide insight into the mechanism of action of a typical interfacial enzyme, a secreted PLA<sub>2</sub>.

### 3.2. Selective Hydrolysis of Lipids by PLA<sub>2</sub>

Secreted PLA<sub>2</sub>s are medium-sized (13–16 kDa) extracellular enzymes that hydrolyze the *sn*-2 acyl chain of glycerophospholipids of cell membranes and liberate unsaturated fatty acids, in particular arachidonic acid, and lyso-phospholipid. These products serve as precursors for the biosynthesis of various eicosanoids or platelet-activating factor, respectively, that possess multiple biological activities, including cell signaling, apoptosis, inflammation, allergy, and tumorigenesis. Secreted PLA<sub>2</sub>s do not have special membrane binding or activation domains like many other interfacial enzymes, although an interfacial adsorption surface has been identified for each isoform. They bind to the cellular plasma membrane in a unique, “productive” mode that results in enzyme activation.<sup>94</sup> One of the factors that facilitate this process of interfacial activation of cationic PLA<sub>2</sub>s is the presence of anionic lipids in the membrane.<sup>96</sup> To understand whether the elevated enzyme activity results from more efficient binding of the cationic protein to the negatively charged membrane surface or from higher intrinsic activity of the enzyme towards the anionic lipid, ATR-FTIR experiments have been conducted on lipid bilayers composed of an equimolar mixture of a zwitterionic lipid dipalmitoylphosphatidylcholine (DPPC) with uniformly perdeuterated acyl chains, DP(d<sub>62</sub>)PC, and an unlabeled anionic lipid dipalmitoylphosphatidylglycerol (DPPG). In an ATR-FTIR experiment, the sample, in this case a lipid bilayer, is deposited on a germanium plate (Figure 1). The incident light is directed into the germanium IRE at one edge with the aid of a set of mirrors and travels to the other edge by means of a series of internal reflections. At each internal reflection, an evanescent wave is created above the surface of the IRE that is absorbed by the sample deposited on it.

As described in section 2.3, deuteration of the lipid acyl chains of DP(d<sub>62</sub>)PC results in a >700 cm<sup>-1</sup> downshift of the methylene stretching vibrational frequency thereby producing FTIR spectra with well-resolved signals from the acyl chains of both unlabeled and deuterated lipids (Figure 2a). The CD<sub>2</sub> absorbance band displays lower intensity and larger width compared to the CH<sub>2</sub> band, consistent with earlier observations.<sup>60</sup> Addition of PLA<sub>2</sub> results in hydrolysis of both lipids and removal of a fraction of the reaction products (free fatty acid and lyso-phospholipid) from the membrane, as evidenced by the reduction of the methylene stretching absorbance intensities. This is consistent with removal of >30% of the bilayer material from membranes caused by lipid hydrolysis by snake venom PLA<sub>2</sub>s.<sup>97-99</sup> A plot of the normalized intensities of the methylene stretching bands versus PLA<sub>2</sub> concentration indicates



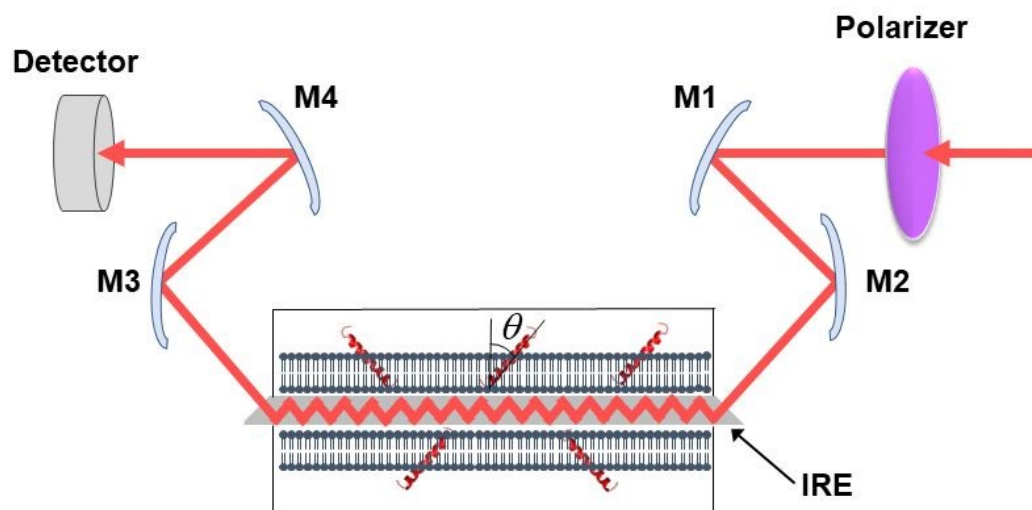


**Figure 1.** Schematic presentation of the ATR-FTIR setting. The infrared light is plane-polarized via a polarizer and directed into the internal reflection element by mirrors M1 and M2. The incident light performs a series of internal reflections, exits the IRE and is directed to the detector by mirrors M3 and M4. The lipid membrane with embedded protein, shown as a single helix, is deposited at both surfaces of the IRE. Reproduced from ref. 94, with permission.

that both the zwitterionic and the acidic lipids are hydrolyzed to similar extents at a given  $\text{PLA}_2$  concentration (Figure 2b). Thus, the result of this isotope-edited ATR-FTIR experiment implies that the higher enzymatic activity of  $\text{PLA}_2$  towards membranes containing negatively charged lipid(s) stems from a stronger electrostatic attraction between the enzyme and the membrane rather than from the intrinsic preference of the enzyme for the anionic lipid.<sup>19</sup>

$\text{PLA}_2$  activity depends on the presence of the reaction products, i.e. the free fatty acid and the lysolipid, in the membrane. The membrane binding affinity as well as the burst activation of  $\text{PLA}_2$  following the initial lag period positively correlated with the presence of lipid hydrolysis products.<sup>100-103</sup> Some studies suggested retention of the reaction products in the membrane<sup>100,101</sup> while others demonstrated removal of a significant fraction of both products from the membrane upon hydrolysis by  $\text{PLA}_2$ .<sup>97-99</sup> Isotope-edited FTIR has been used to determine whether both products of lipid hydrolysis dissociate from the membrane after lipid hydrolysis to equal extents or one of them preferentially accumulates in the membrane and plays a prevalent role in  $\text{PLA}_2$  activity.  $\text{PLA}_2$  was applied to supported membranes of DPPC with perdeuterated *sn*-1 chain and unlabeled *sn*-2 chain (Figure 3a). In this case, the  $>700\text{ cm}^{-1}$  separation of the methylene stretching vibrational signals provided spectral resolution of both acyl chains and thereby allowed monitoring the removal of each chain from the membrane upon lipid hydrolysis (Figure 3b). As shown in Figure 3c, while both  $\text{CH}_2$  and  $\text{CD}_2$  signals monotonously decrease with increasing  $\text{PLA}_2$  concentration, the reduction in the  $\text{CD}_2$  signals, which represents the lysophospholipid containing the *sn*-1 chain, prevails that of the  $\text{CH}_2$  signals, which represents the free fatty acid. This result implies that the free fatty acid preferentially accumulates in the membrane following hydrolysis by  $\text{PLA}_2$  and may modulate the enzyme's function by affecting the membranes surface charge and the structure.



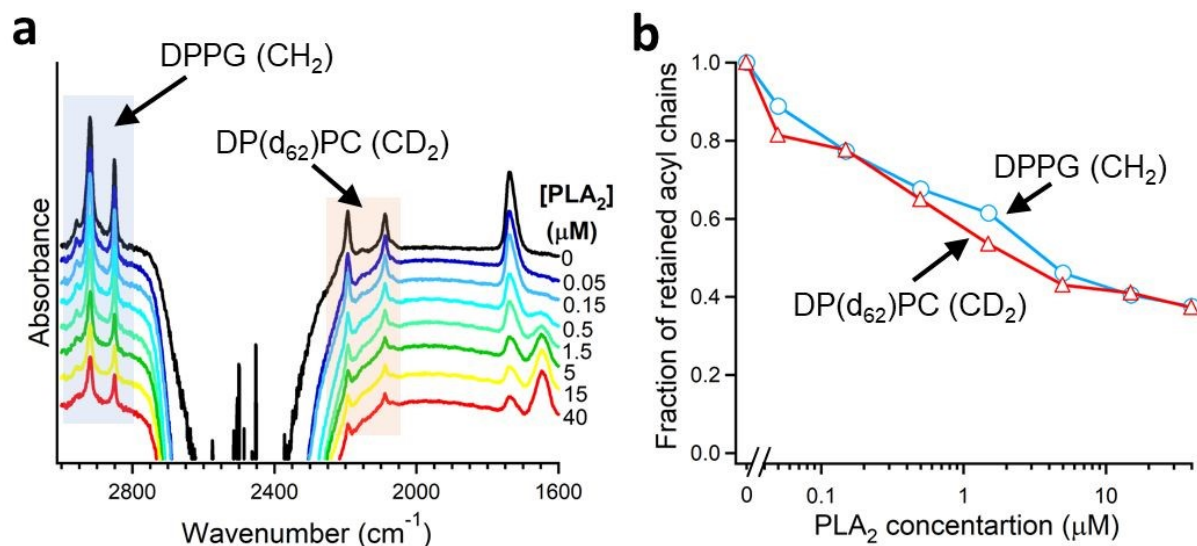
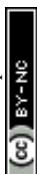


**Figure 2.** Hydrolysis of the two components of a binary lipid bilayer by PLA<sub>2</sub>. (a): ATR-FTIR spectra of a lipid bilayer composed of an equimolar combination of DPPG and chain-perdeuterated DP(d<sub>62</sub>)PC at different concentrations of PLA<sub>2</sub>, as indicated. (b): Dependence of the integrated methylene absorbance intensities of both lipids on PLA<sub>2</sub> concentration. Adapted from ref. 19, with permission.

### 3.3. Positioning of PLA<sub>2</sub> with Respect to the Membrane

As mentioned above, interfacial enzymes are activated by binding to biomembranes and forming a protein-membrane complex of highly specific configuration, including the depth of membrane insertion and the geometric orientation of the protein with respect to the membrane. For enzymes that use a membrane lipid as substrate, such as various PLA<sub>2</sub> isoforms, this specific configuration is a prerequisite for efficient enzyme function as it determines the strength of membrane binding and the mode of substrate accession and product release, i.e. the most important steps of the whole catalytic cycle.<sup>104</sup> Determination of the positioning of a secreted PLA<sub>2</sub> on a lipid membrane has been achieved by combination of protein engineering, isotope-edited FTIR, and fluorescence spectroscopy, as described below.

As shown in Figure 1, the orientation of a molecule that has a rotational axis of symmetry, such as a helix, can be determined by polarized ATR-FTIR spectroscopy. Briefly, the spectra obtained with infrared light polarized coplanar and orthogonal to the plane of incidence are used to determine the dichroic ratio, i.e. the ratio of absorbances at two polarizations. The measured dichroic ratio, together with known parameters such as the angle of the helical amide I transition dipole with respect to the helical axis ( $39^{\circ} \pm 1^{\circ}$ ), the Cartesian electric vector components of the evanescent wave, and the refractive indices of the IRE, the membrane, and the bathing solution, allow determination of the helical order parameter which directly provides the average orientation of the helix relative to the membrane (angle  $\theta$  in Figure 1).<sup>18,105</sup> Determination of the orientation of a protein of irregular shape is not trivial, however, as the protein may have multiple helices of arbitrary orientations. It has been shown that determination of the orientation of the whole protein requires the orientations of at least two different helices.<sup>106</sup> Human pancreatic PLA<sub>2</sub> has been chosen to solve the problem because it is a relatively simple protein



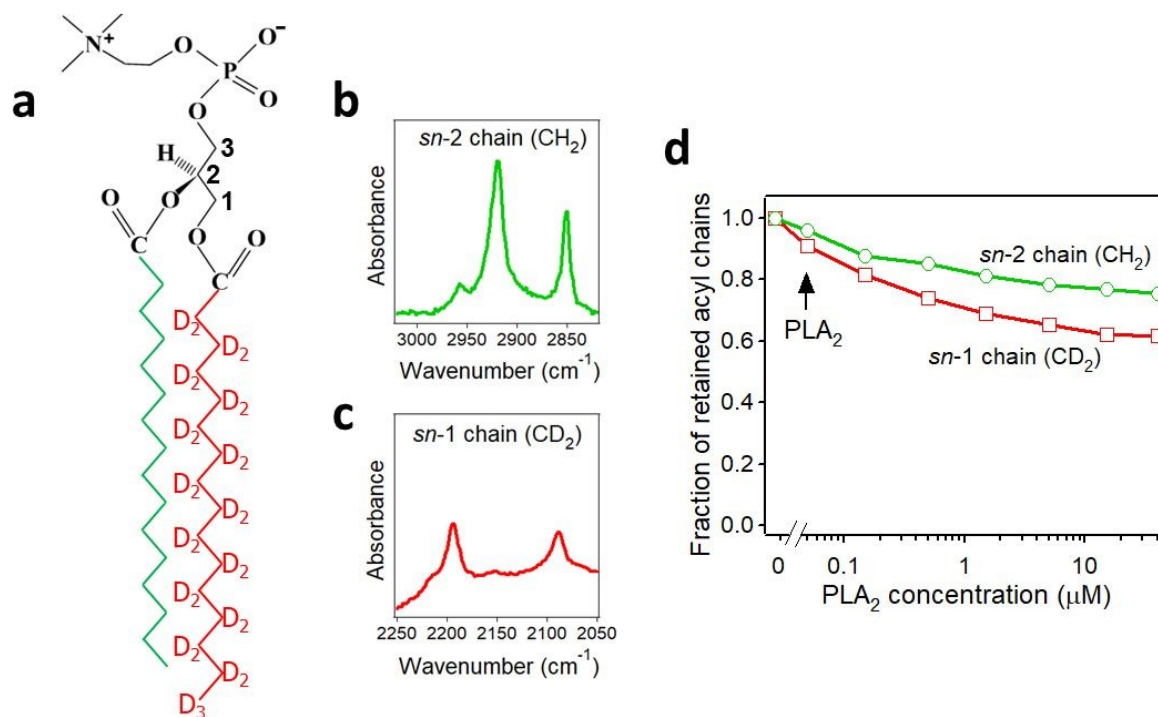


**Figure 3.** Hydrolysis of the acyl chains of DPPC with deuterated *sn*-1 chain and unlabeled *sn*-2 chain by PLA<sub>2</sub>. (a): Structure of DPPC with deuterated *sn*-1 chain (red) and unlabeled *sn*-2 chain (green). (b) and (c): The methylene stretching bands of the unlabeled (b) and deuterated (c) acyl chains of the lipid. (d): Dependence of the integrated methylene absorbance intensities of the unlabeled (green) and deuterated (red) acyl chains on PLA<sub>2</sub> concentration. Adapted from ref. 19, with permission.

with three  $\alpha$ -helices, an N-terminal helix (residues 1-10) and two internal helices. A semisynthetic, segmentally <sup>13</sup>C-labeled PLA<sub>2</sub> was produced where an unlabeled synthetic peptide corresponding to the N-terminal helix, with a thioester functional group at the C-terminus, was ligated to a uniformly <sup>13</sup>C-labeled construct corresponding to the rest of the protein.<sup>106</sup> The residue 11 (the first residue of the <sup>13</sup>C-labeled construct) is a cysteine and is ideally located for thioester-to-cysteine peptide ligation (Figure 4). Analysis of the protein structure showed that the two internal helices were nearly antiparallel, so, in terms of orientation, the protein could be treated as a two-helix system (in ATR-FTIR, parallel and antiparallel orientations are equivalent). ATR-FTIR spectra with coplanar and orthogonal polarizations of the incident light produced multicomponent amide I bands, with the components generated by the unlabeled N-terminal helix and the two <sup>13</sup>C-labeled internal helices located at 1656 and 1616 cm<sup>-1</sup>, respectively (Figure 5a,b). These data, along with specially developed analytic geometry algorithms, allowed determination of the orientations of the helices and hence of the whole protein relative to the membrane. The depth of membrane insertion was determined by experiments of quenching of the fluorescence of the single tryptophan-3 of pancreatic PLA<sub>2</sub> by lipids brominated at various positions along the acyl chains. Isotope-edited polarized ATR-FTIR and fluorescence data thus produced the structure of the protein-membrane complex with a unique positioning of the protein on the membrane in terms of geometric configuration and depth of membrane insertion (Figure 5c).<sup>106</sup>



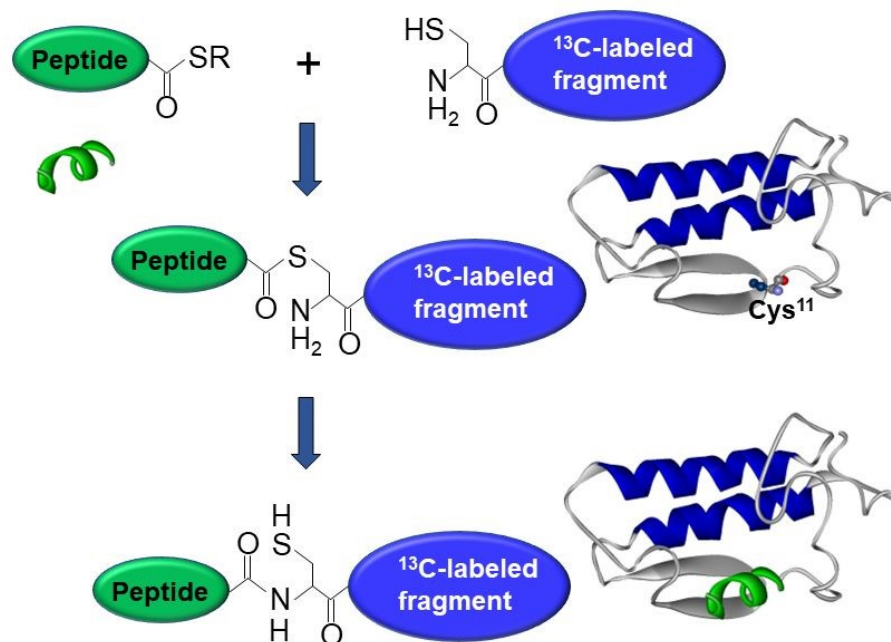


**Figure 4.** Graphical description of the thioester-cysteine chemical ligation. The synthetic unlabeled peptide (green) with a C-terminal thioester group reacts with the thiol of the N-terminal cysteine of a recombinant, uniformly  $^{13}\text{C}$ -labeled protein fragment (blue) followed by S-to-N acyl transfer and formation of a natural peptide bond, resulting in a semisynthetic, segmentally isotope-labeled protein. Adapted from ref. 18, with permission.

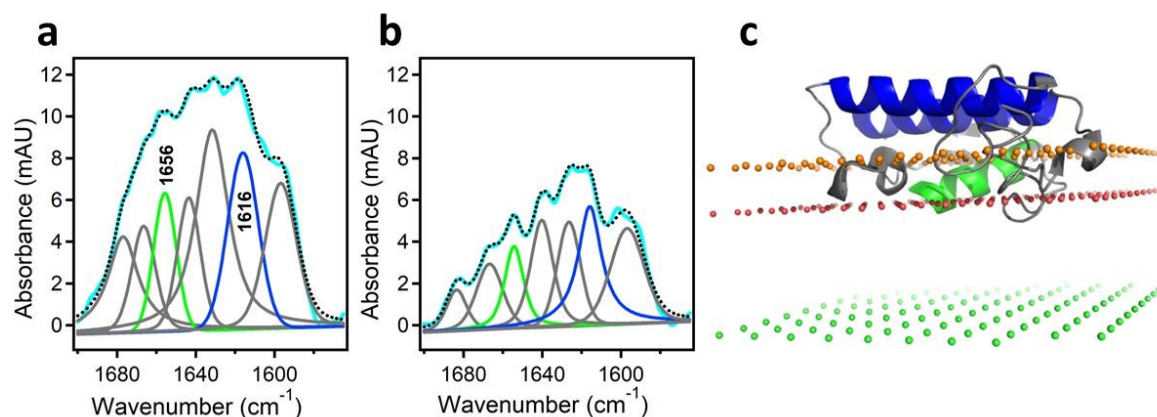
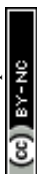


**Figure 5.** Determination of the orientation of a membrane-bound protein by polarized ATR-FTIR spectroscopy. (a) and (b): ATR-FTIR spectra of membrane-bound human pancreatic  $\text{PLA}_2$  with unlabeled N-terminal helix and  $^{13}\text{C}$ -labeled fragment at coplanar (a) and orthogonal (b) polarizations of the incident light with respect to the plane of incidence. The measured spectrum is shown in cyan and the sum of all amide I components is shown as dotted black line. The amide I components generated by the unlabeled and  $^{13}\text{C}$ -labeled helices are shown in green and blue, respectively. (c): The structure of the protein bound to the membrane with its N-terminal and internal helices shown in green and blue, respectively. The three planes indicate the locations of the membrane center (green), the *sn*-1 carbonyl oxygens (red) and the phosphate atoms (orange) of the lipid. Adapted from ref. 106, with permission.





In this structure, the  $z$  coordinate of each atom of the protein is its distance from the membrane center so the location of each amino acid can be easily pinpointed. The protein was found to significantly penetrate into the membrane hydrocarbon core, with tryptophan-3 located at  $9 \pm 1$  Å from the membrane center and providing a hydrophobic anchor for membrane docking of PLA<sub>2</sub> together with phenylalanine-19 and leucine-20. Penetration of a cobra venom PLA<sub>2</sub> into phosphatidylcholine bilayers 5-7 Å below the lipid headgroup plane has been reported,<sup>99</sup> in good agreement with this finding. In addition to hydrophobic interactions, several cationic amino acid residues were involved in H-bonding with lipid carbonyl oxygens or in ionic interactions with lipid phosphate groups. Inspection of the structure shown in Figure 5c indicates that the opening of the substrate-binding cleft faces the membrane surface so that the catalytic histidine-48 is located at  $\sim 7$  Å from the *sn*-2 ester group of the glycerophospholipid allowing the lipid to travel a shorter distance to reach the catalytic site compared to  $\sim 15$  Å proposed earlier.<sup>107,108</sup> Thus, this technique, where isotope-edited FTIR plays a central role, provides an efficient tool to elucidate the mode of membrane binding of a peripheral protein and the mechanism of its action.

## 4. PROTEIN-PROTEIN INTERACTIONS

### 4.1. Overview and Importance of Protein-Protein Interactions

Protein-protein interactions play crucial roles in cell function by supporting vitally important biomolecular structures or processes. In fact, from 300,000 to 650,000 promiscuous protein-protein interactions are involved in human physiology.<sup>2</sup> Protein assemblies can be divided into two classes, i.e., stable multiprotein structures that serve specific functions and transient complexes that are mostly involved in the dynamic events of cell signaling.<sup>1,3</sup> Interactions between protein subunits are facilitated by a combination of nonspecific (hydrophobic, ionic, H-bonding) and specific (e.g., shape-complementary, hand-in-glove- or lock-and-key-type) contacts between domains and motifs that often contain critically important “hot spot” amino acids.<sup>1,3,81,109-111</sup> As an antithesis of the lock-and-key interactions between (relatively) rigid domains, the “induced fit” or “folding-upon-binding” interactions between initially flexible protein modules such as antibodies or receptors or their ligands that acquire defined shape upon interaction result in promiscuity and polyreactivity effects of profound biological importance.<sup>3,112-116</sup>

The transient complexes between proteins are formed through highly specific interactions of moderate affinity (typically, nanomolar to micromolar dissociation constants).<sup>117-119</sup> Important examples of transient protein-protein complexes are the enzyme-substrate,<sup>117-120</sup> enzyme-inhibitor,<sup>121,122</sup> ligand-receptor,<sup>123-125</sup> and antigen-antibody interactions.<sup>3,111,126</sup> More than 100 signaling proteins in human genome contain one or more Src homology 2 domain(s) that mediate binding to phosphorylated tyrosine involved in signal transduction.<sup>127</sup> Other protein modules such as the PDZ domain, breast cancer susceptibility protein 1, forkhead-associated domain, mad homology domain 2, interferon regulatory factor 3, polo-box domain unique to the polo-like kinases, the FF, WW, and WD40 motifs containing the respective dipeptides mediate the transient binding of signaling molecules to phosphoserine or phosphothreonine.<sup>2,128</sup> The 14-3-3 family proteins bind to and regulate around 1,200 partners involved in a plethora of cellular functions and are regulated themselves by caspase-mediated proteolysis, lysine acetylation, or serine/threonine phosphorylation.<sup>2,129</sup> The Src homology 3 (SH3) domain, on the other hand, binds proline-rich protein motifs that fit into a groove on the surface of the SH3 domain.<sup>130</sup>



Finally, regulatory (effector) proteins up- or down-regulate the activity of enzymes or switch from one to another function of multidomain modular proteins via interacting with an allosteric site.<sup>131</sup>

A special type of protein-protein interactions is aggregation of misfolded proteins and formation of amyloid fibrils that are involved in many pathologies. Some prominent examples are involvement of the amyloid  $\beta$  ( $A\beta$ ) and tau proteins in Alzheimer's disease,  $\alpha$ -synuclein in Parkinson's disease, prion protein in Creutzfeldt-Jakob disease, insulin in iatrogenic amyloidosis, immunoglobulin light chain and transthyretin in cardiac amyloidosis and polyneuropathy, islet amyloid polypeptide (amylin) in type II diabetes, hemoglobin in sickle cell anemia etc.<sup>132-141</sup> Amyloidogenesis occurs with or without genetic, inheritable mutations in the respective protein, and the fibrils display remarkable structural similarities, such as formation of the cross- $\beta$ -sheet structure, despite the absence of sequence similarities.<sup>137,140</sup>

The importance of protein-protein interactions in cell physiology has led the researchers to develop multiple methods to analyze protein complex formation and the structure and function of the complexes. An incomplete list of these methods includes the yeast two-hybrid system, the protein-fragment complementation assay, fluorescence resonance energy transfer, co-immunoprecipitation, tandem affinity purification coupled to mass spectrometry, (in-cell) cross-linking mass spectrometry, (in-cell) single-molecule tracking, stable isotope labeling by amino acids in cell culture, and computational (in silico) methods.<sup>110,142-149</sup> Described in the following sections are the use of isotope-edited FTIR to analyze the structural aspects of  $A\beta$  fibrillogenesis and the regulation of sarcoplasmic reticulum (SR)  $Ca^{2+}$ -ATPase by phospholamban (PLB).

## 4.2. Protein Aggregation

The  $A\beta$  peptide aggregates constitute a histopathological hallmark of the Alzheimer's disease (AD).<sup>150</sup>  $A\beta$  is derived from the amyloid precursor protein, a bitopic protein in neuronal membranes, and represents mostly its  $\alpha$ -helical transmembrane part. Upon enzymatic cleavage and exposure to aqueous medium, the peptide undergoes transition to  $\beta$ -sheet structure followed by fibrillogenesis.  $A\beta$  occurs in various forms in human brain in terms of the number of amino acids and enzymatic modifications; in addition to the prevalent 40- and 42-residue species ( $A\beta_{1-40}$ ,  $A\beta_{1-42}$ ), N-terminally truncated and pyroglutamylated forms ( $A\beta_{pE3-40}$ ,  $A\beta_{pE3-42}$ ) are present as well and are hypertoxic.<sup>37</sup> Since in human brain these peptides are intermixed and undergo aggregation into hetero-complexes, it is of interest to understand the structural changes in each species during aggregation and the mutual structural effects. Isotope-edited FTIR has been used to achieve this goal.

The synthetic, lyophilized, uniformly  $^{13}C$ -labeled  $A\beta_{1-42}$  and unlabeled  $A\beta_{pE3-42}$  peptides were dissolved in hexafluoroisopropanol to disperse possible aggregates and were dried on a  $CaF_2$  FTIR window. These samples generated amide I spectra with peaks around  $1617\text{ cm}^{-1}$  and  $1658\text{ cm}^{-1}$  and amide II peaks around  $1533\text{ cm}^{-1}$  and  $1544\text{ cm}^{-1}$ , respectively (Figure 6a,c, black lines). In view of the  $\sim 40\text{ cm}^{-1}$  downshift due to  $^{13}C$ -labeling, these data indicate  $\alpha$ -helical structure for both peptides before hydration. To observe the kinetics of  $\alpha$ -helix to  $\beta$ -sheet transition upon hydration as well as the intermediate oligomeric forms that are the main toxic



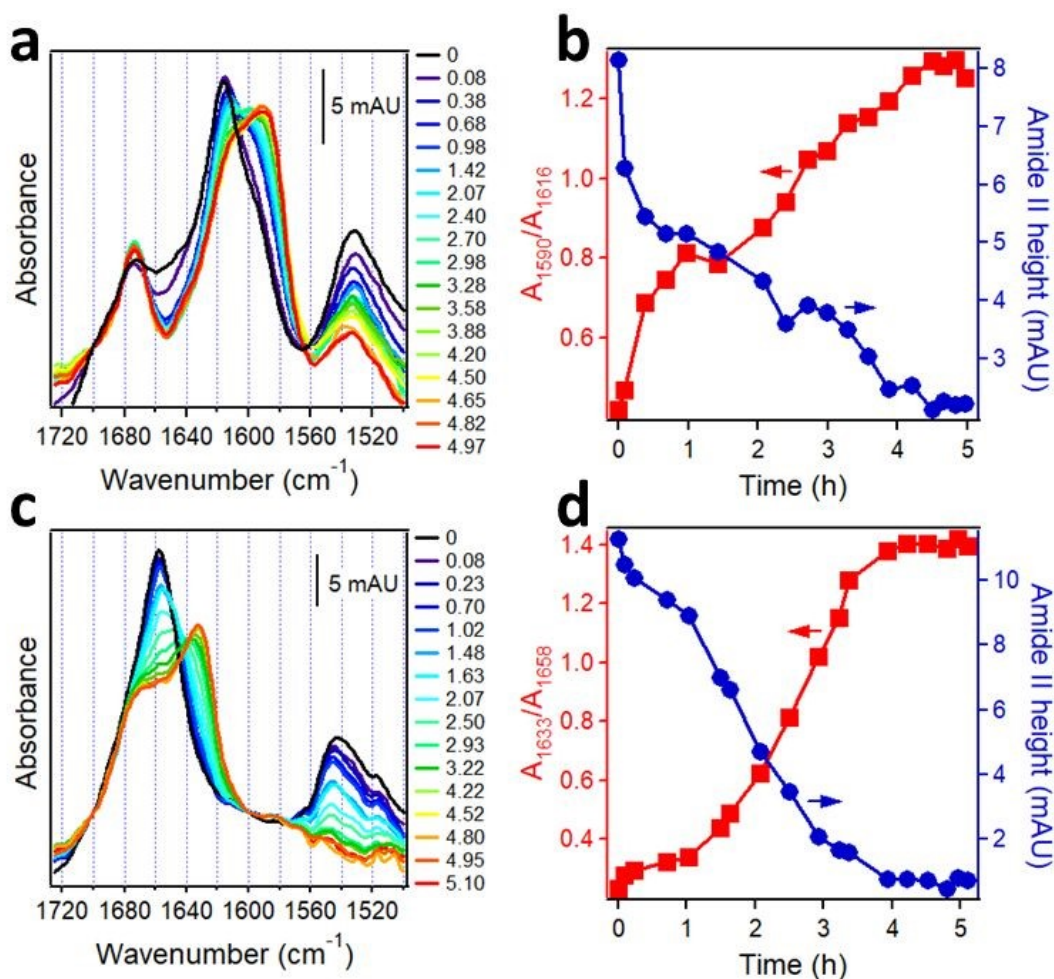


**Figure 6.** Structural changes in Aβ peptides upon hydration with D<sub>2</sub>O-saturated nitrogen gas. FTIR spectra of <sup>13</sup>C-Aβ<sub>1-42</sub> (a) and Aβ<sub>pE3-42</sub> (c) dried on a CaF<sub>2</sub> window (black lines) and upon injection of D<sub>2</sub>O-saturated nitrogen for ~ 5 h (blue to red). Panels a and c are appended with columns indicating time of exposure to D<sub>2</sub>O vapor (in hours). Panels (b) and (d) show the kinetics of β-sheet structure formation in <sup>13</sup>C-Aβ<sub>1-42</sub> (b) and Aβ<sub>pE3-42</sub> (d) (red) and change in amide II intensities (blue) as a function of time of exposure to D<sub>2</sub>O vapor. Adapted from ref. 37, with permission.

species, the structural change was slowed down by pumping D<sub>2</sub>O-saturated nitrogen gas into the chamber of the spectrometer allowing measurements at distinct stages of the transition.

Hydration with D<sub>2</sub>O vapor resulted in gradual shift of the α-helical peaks to 1588 cm<sup>-1</sup> for <sup>13</sup>C-Aβ<sub>1-42</sub> and to 1632 cm<sup>-1</sup> for Aβ<sub>pE3-42</sub>, indicating α-helix to β-sheet transition of both proteins (Figure 6a, c). Concomitantly, the intensity in the initial (non-deuterated) amide II band declined because of the downshift of the deuterated amide II mode by ~90 cm<sup>-1</sup> (see Introduction). The kinetics of the HX, i.e. the time-dependence of amide II intensity, and of the α-helix-β-sheet transition, i.e. the ratio of absorbance intensities of the β-sheet and α-helical amide I signals, are shown in Figure 6b, d. <sup>13</sup>C-Aβ<sub>1-42</sub> readily underwent amide HX and α-helix to β-sheet transition once exposed to D<sub>2</sub>O vapor (Figure 6b) but the peptide was not entirely amide-deuterated after 5 hours of exposure to D<sub>2</sub>O vapor as indicated by the residual amide II intensity (red line in Figure 6a and blue line in Figure 6b), indicating partial solvent protection possibly due to a compact



tertiary structure.  $A\beta_{pE3-42}$  behaved differently. Despite the significant decrease in the amide II intensity during the first 1.0-1.5 hours of deuteration, indicative of extensive HX, the peptide initially experienced little structural changes (Figure 6d). Following the lag period, the peptide underwent  $\alpha$ - $\beta$  transition in a sigmoidal manner, yet a significant fraction of the initial  $\alpha$ -helix as well as  $\beta$ -turn structure persisted after the transition leveled off (shoulder around 1677-1658  $\text{cm}^{-1}$  of the red spectrum of Figure 6c). In contrast to  $^{13}\text{C-A}\beta_{1-42}$ , nearly all amide protons of  $A\beta_{pE3-42}$  exchanged for deuterium, as indicated by the reduction of the amide II signal to zero (Figure 6c), suggesting a more open, solvent-exposed tertiary fold. This result is consistent with recently published fluorescence data showing solvent-inaccessibility of tyrosine-10 of  $A\beta_{1-42}$  and solvent exposure of same residue of  $A\beta_{pE3-42}$ .<sup>151</sup>

Above data uncover distinct structural pathways of  $\alpha$ -helix to  $\beta$ -sheet structural transitions of the unmodified and pyroglutamylated  $A\beta$  peptides, i.e., resistance of the latter to transition to  $\beta$ -sheet structure and a less compact tertiary fold. However, in brain tissue and in the extracellular plaques various forms of  $A\beta$  are blended and may affect each other's structural behavior. Such mutual structural effects have been analyzed as follows.  $A\beta_{pE3-42}$  and  $^{13}\text{C-A}\beta_{1-42}$  have been dissolved in hexafluoroisopropanol and deposited separately on the opposite sides of a  $\text{CaF}_2$  FTIR window as well as mixed at 1:1 molar ratio and deposited on the same side of another  $\text{CaF}_2$  window. These two samples were dried by desiccation and mounted on two mutually orthogonal vertical faces of a rotatable stage and placed in the spectrometer. Consecutive FTIR spectra of both separate and combined samples were measured alternately by turning the stage back and forth by 90 degrees about a 4-fold vertical axis while the chamber was purged with  $\text{D}_2\text{O}$ -saturated nitrogen. The difference between these spectra at a given time point, i.e. at a given level of amide deuteration, then revealed the mutual structural effects.<sup>37</sup>

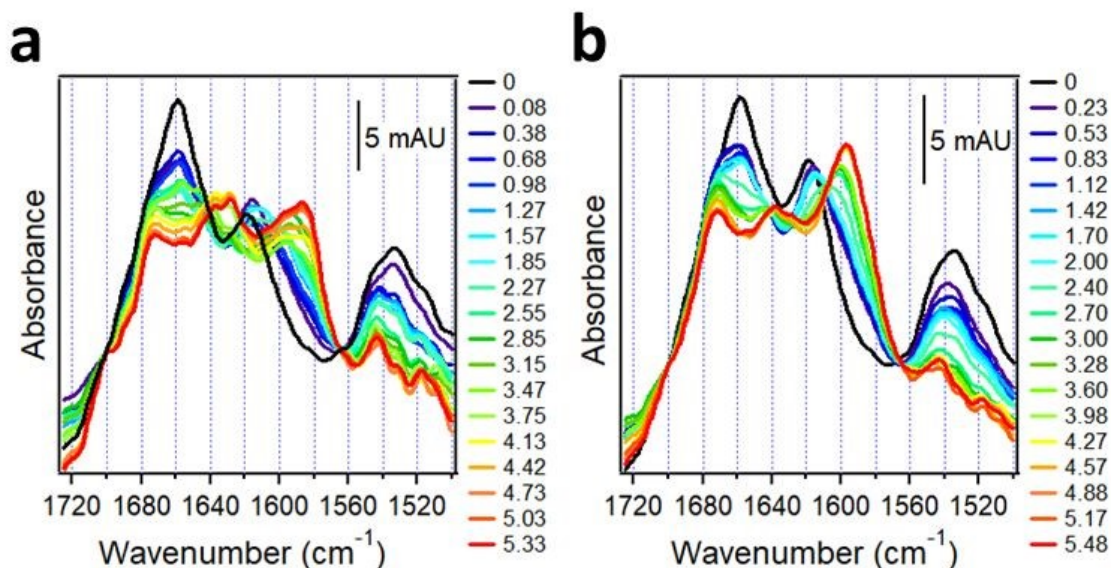


**Figure 7.** Structural changes in  $^{13}\text{C-A}\beta_{1-42}$  and  $A\beta_{pE3-42}$  upon hydration with  $\text{D}_2\text{O}$ -saturated nitrogen gas when physically separated (a) and combined at 1:1 molar ratio (b). Both panels are appended with columns indicating time of exposure to  $\text{D}_2\text{O}$  vapor (in hours). Reproduced from ref. 37, with permission.



These samples generated complex spectra incorporating the features of both unlabeled and  $^{13}\text{C}$ -labeled peptides. In the isolated system, both  $^{13}\text{C}$ -A $\beta_{1-42}$  and A $\beta_{pE3-42}$  were  $\alpha$ -helical in dry state indicated by the amide I peaks around  $1618\text{ cm}^{-1}$  and  $1658\text{ cm}^{-1}$ , respectively (black line in Figure 7a). The weaker amide I intensity of  $^{13}\text{C}$ -A $\beta_{1-42}$  is consistent with observations of 20-30% lower amide I peak heights of  $^{13}\text{C}$ -labeled helical peptide segments compared to the unlabeled segments.<sup>30</sup> Hydration by  $\text{D}_2\text{O}$  vapor transformed the spectra and produced downshifted peaks at  $1586\text{ cm}^{-1}$  and  $1628\text{ cm}^{-1}$  with higher frequency shoulders located at  $1597\text{ cm}^{-1}$  and  $1639\text{ cm}^{-1}$  (red line in Figure 7a). The strong signal at  $1586\text{ cm}^{-1}$  and  $1628\text{ cm}^{-1}$  is readily assigned to intermolecular  $\beta$ -sheet structure in  $^{13}\text{C}$ -A $\beta_{1-42}$  and A $\beta_{pE3-42}$ , respectively, while the upshifted weaker signal at  $1597\text{ cm}^{-1}$  and  $1639\text{ cm}^{-1}$  indicates a smaller fraction of  $\beta$ -sheet with intramolecular H-bonding.<sup>18,152</sup> An additional peak around  $1673\text{ cm}^{-1}$  can be assigned to  $\beta$ -turn structure in A $\beta_{pE3-42}$ .

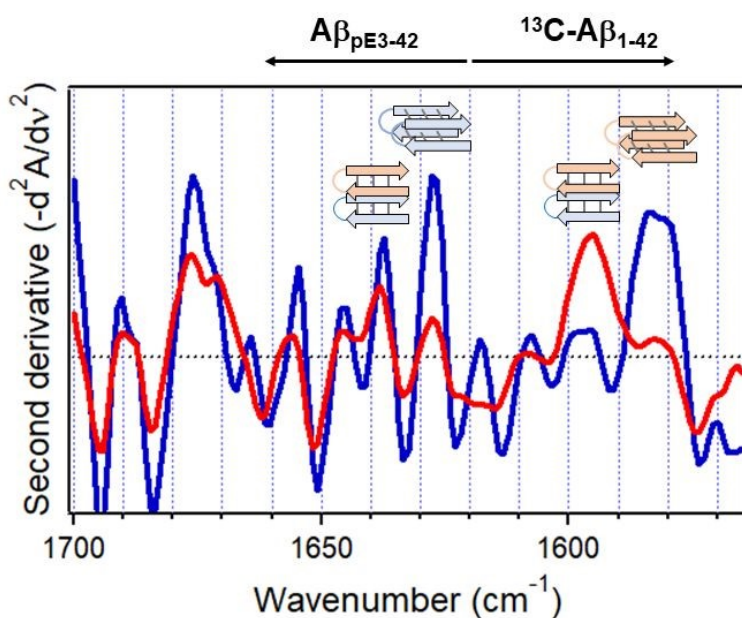


**Figure 8.** Inverted second derivative amide I spectra of  $^{13}\text{C}$ -A $\beta_{1-42}$  and A $\beta_{pE3-42}$  after 5 h hydration with  $\text{D}_2\text{O}$ -saturated nitrogen gas when physically separated (blue) and combined at 1:1 molar ratio (red). Cartoons for homo- or hetero-oligomers stabilized by intermolecular and intramolecular H-bonding, respectively, are shown above respective spectral features ( $^{13}\text{C}$ -A $\beta_{1-42}$ , rose, and A $\beta_{pE3-42}$ , blue). Reproduced from ref. 37, with permission.

Spectra of the combined  $^{13}\text{C}$ -A $\beta_{1-42}$ /A $\beta_{pE3-42}$  sample hydrated by  $\text{D}_2\text{O}$  vapor displayed a stronger higher frequency signal assigned to intramolecular H-bonded  $\beta$ -sheet and a weaker lower frequency, intermolecular H-bonded  $\beta$ -sheet signal (red line in Figure 7b). In fact, the signal at  $1586\text{ cm}^{-1}$  assigned to the intermolecular  $\beta$ -sheet of  $^{13}\text{C}$ -A $\beta_{1-42}$  was not present in the combined peptide sample at all. These spectral effects can be amplified by resolution enhancement techniques. The second derivative spectra shown in Figure 8 identify strong signals of the isolated sample located at  $1584\text{ cm}^{-1}$  and  $1627\text{ cm}^{-1}$  and weaker signal around  $1597\text{ cm}^{-1}$  and  $1537\text{ cm}^{-1}$  (blue line of Figure 8) signifying larger fractions of aggregates with intermolecular H-bonding for both  $^{13}\text{C}$ -A $\beta_{1-42}$  and A $\beta_{pE3-42}$ . In the spectrum of the combined



sample, the relative intensities of these signals was reversed (red line of Figure 8), indicating conversion of the intermolecular H-bonded aggregates to  $\beta$ -sheet structures stabilized by intramolecular H-bonding, as schematically shown above the respective spectral features in Figure 8. These data identify mutual structural effects of the unmodified and pyroglutamylated A $\beta$  peptides, i.e., diversion of the aggregation process from fibril formation stabilized by intermolecular H-bonding to oligomeric structures of hairpin-like  $\beta$ -sheets that may exert a stronger cytotoxic effect as the oligomers are more toxic than the fibrils.<sup>37,141,153-155</sup> This is an example of how isotope-edited FTIR spectroscopy can provide insight into the molecular mechanism of disease such as AD.

### 4.3. In-membrane Protein-Protein Interactions

Described in this section is the use of isotope-edited FTIR spectroscopy to analyze the regulatory interaction between two membrane proteins, i.e., regulation of the activity of SR  $\text{Ca}^{2+}$ -ATPase by PLB that plays a central role in the contraction-relaxation cycle of heart muscle.<sup>156</sup> Excitation of the cardiomyocyte triggers  $\text{Ca}^{2+}$  influx through the voltage-sensitive  $\text{Ca}^{2+}$  channels, which in turn activates the type-2 ryanodine receptor  $\text{Ca}^{2+}$  channels in the SR membrane resulting in additional increase in the cytosolic  $\text{Ca}^{2+}$  level and contraction by the  $\text{Ca}^{2+}$ -sensitive contractile proteins. This is followed by relaxation that takes place mainly by pumping the cytosolic  $\text{Ca}^{2+}$  back into the SR lumen by the SR  $\text{Ca}^{2+}$ -ATPase. The activity of the  $\text{Ca}^{2+}$ -ATPase is regulated by PLB, a relatively small bitopic protein in the SR membrane, as schematically shown in Figure 9a. Specifically, PLB moderates the enzymatic activity of the  $\text{Ca}^{2+}$ -ATPase and phosphorylation of PLB by cAMP- and/or  $\text{Ca}^{2+}$ /calmodulin-dependent protein kinases ceases the inhibitory effect.<sup>157-159</sup> Various forms of cardiomyopathy in humans are associated with reduction of the levels of both the SR  $\text{Ca}^{2+}$ -ATPase and PLB at mRNA and protein levels.<sup>156</sup> The regulatory

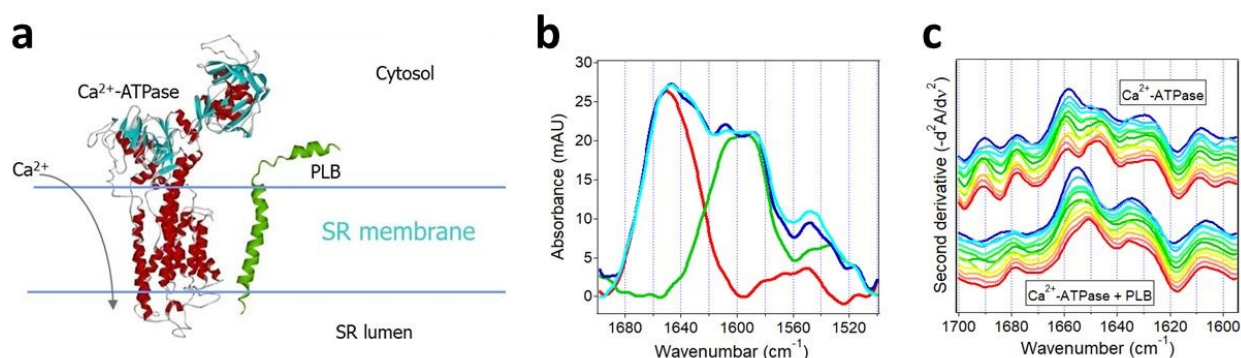


**Figure 9.** Structural effects resulting from interaction of SR  $\text{Ca}^{2+}$ -ATPase with uniformly  $^{13}\text{C}$ -labeled PLB. (a): Cartoon for the  $\text{Ca}^{2+}$ -ATPase and PLB in the SR membrane. (b): ATR-FTIR spectra of membrane-reconstituted  $\text{Ca}^{2+}$ -ATPase (red), uniformly  $^{13}\text{C}$ -labeled PLB (green), the sum of the spectra of  $\text{Ca}^{2+}$ -ATPase and  $^{13}\text{C}$ -PLB measured separately (blue), and the spectrum of the 1:11 molar combination of  $\text{Ca}^{2+}$ -ATPase and  $^{13}\text{C}$ -PLB (cyan). (c): Inverted second derivative spectra of  $\text{Ca}^{2+}$ -ATPase alone (upper group of curves) and with  $^{13}\text{C}$ -PLB at 11-fold molar excess (lower group of curves). Time of exposure to  $\text{D}_2\text{O}$ -based buffer was 2 min, 4 min, 9 min, 19 min, 36 min, 1 h, 1.4 h, 3 h, 4.4 h, 6 h, and 8 h (blue to red). Partially adopted from ref. 157, with permission.



effect of PLB has been shown to involve direct molecular contact between the ATPase and PLB and several intermolecular interaction sites have been identified but the mechanism of regulation remains unclear.<sup>158-160</sup>

Since PLB exerts similar regulatory effects on both the cardiac and skeletal muscle SR Ca<sup>2+</sup>-ATPases and the latter maintains higher functional stability following purification, ATR-FTIR studies have been carried out on recombinant, uniformly <sup>13</sup>C-labeled PLB and skeletal muscle SR Ca<sup>2+</sup>-ATPases co-reconstituted in supported membranes composed of SR-extracted lipids.<sup>157</sup> First, spectra of each membrane-embedded protein were measured separately. The Ca<sup>2+</sup>-ATPase generated amide I and amide II bands centered at 1658 cm<sup>-1</sup> and 1546 cm<sup>-1</sup>, respectively (red line in Figure 9b). The strong signal at 1658 cm<sup>-1</sup> is consistent with the mostly  $\alpha$ -helical secondary structure of the Ca<sup>2+</sup>-ATPase (Figure 9a). <sup>13</sup>C-PLB produced a wide amide I band composed of two components at 1608 cm<sup>-1</sup> and 1585 cm<sup>-1</sup> indicating  $\alpha$ -helical and  $\beta$ -sheet structures, in accord with earlier FTIR studies,<sup>161</sup> and an amide II band at 1525 cm<sup>-1</sup> (green line in Figure 9b). The 50 cm<sup>-1</sup> spectral shift between the  $\alpha$ -helical amide I modes of the two proteins is consistent with the expected isotopic effect.

The spectrum of the Ca<sup>2+</sup>-ATPase and <sup>13</sup>C-PLB co-reconstituted at 11:1 PLB:ATPase molar ratio displayed the structural features of both proteins (cyan line in Figure 9b). A resolution enhancement procedure, i.e. second derivative spectral analysis in the amide I region of Ca<sup>2+</sup>-ATPase, was conducted to discern structural effects exerted by PLB. Time-dependent changes in the second derivative spectra over an 8 hour period unveiled interesting effects. In the initial stages of exposure of the proteins to D<sub>2</sub>O, a strong component at 1658 cm<sup>-1</sup> and weaker one at 1647 cm<sup>-1</sup> were present in the spectrum of the Ca<sup>2+</sup>-ATPase (Figure 9c, upper family of curves), which can be readily assigned to non-deuterated and deuterated  $\alpha$ -helices.<sup>18</sup> By 8 hours of exposure to D<sub>2</sub>O, the relative intensities of these components switched toward a larger fraction of the deuterated helices. The spectral features in the 1637-1625 cm<sup>-1</sup> and 1700-1670 cm<sup>-1</sup> regions represent  $\beta$ -sheet and turn structures while those below 1610 cm<sup>-1</sup> are assigned to side chains. In the presence of PLB, the  $\alpha$ -helical signal at 1658 cm<sup>-1</sup> was downshifted by 3-4 cm<sup>-1</sup> and its further downshift due to deuteration occurred much slower (Figure 9c, lower family of curves). Both effects suggest stabilization of the  $\alpha$ -helices of Ca<sup>2+</sup>-ATPase upon interaction with PLB. More stable helices involve stronger intramolecular H-bonding and hence weaker C=O covalent bonds, corresponding to lower vibrational frequency. The stronger C=O...H-N H-bonding, on the other hand, will slow down the amide deuteration, as detected. In addition, the relative intensities of non-deuterated vs. deuterated  $\beta$ -sheets of the Ca<sup>2+</sup>-ATPase (signals around 1637 cm<sup>-1</sup> and 1625 cm<sup>-1</sup>) was shifted toward the former in the presence of PLB, in agreement with overall slower HX. Finally, the more stable structure and less effective HX of the Ca<sup>2+</sup>-ATPase in the presence of PLB was confirmed by a stronger amide II band of the Ca<sup>2+</sup>-ATPase around 1546 cm<sup>-1</sup> as compared to that in the spectral sum of the two proteins measured separately (cf. cyan and blue lines of Figure 9b). The data thus indicate stabilization of the secondary structure of the Ca<sup>2+</sup>-ATPase by PLB with no significant structural changes in PLB itself. These findings offer a mechanism for the inhibitory action of PLB on Ca<sup>2+</sup>-ATPase through increased rigidity of the ATPase structure by PLB and hindrance of the conformational changes involved in the catalytic turnover.

## 5. SITE-SPECIFIC STRUCTURE DETERMINATION

### 5.1. Isotope Labeling Schemes



Data described above indicate the remarkable sensitivity of FTIR spectroscopy to the structural dynamics of proteins. However, FTIR usually provides the global rather than local structural information and hence is considered a “low-resolution” technique. Local, site-specific structure of proteins can be determined by isotope-edited FTIR spectroscopy using proteins that are isotopically labeled at selected amino acid residues. Since the conformation-sensitive amide I mode is produced mostly by the main chain C=O stretching vibration (76%) as well as by the C–N stretching, C–C–N deformation, and N–H in-plane bending modes,<sup>18</sup> the most common labeling schemes include carbonyl <sup>13</sup>C labeling, double <sup>13</sup>C,<sup>15</sup>N-labeling, or double <sup>13</sup>C=<sup>18</sup>O-labeling of main chain atoms, which result in significant spectral shifts and resolution of the targeted site(s), as described in section 2.2.

The incorporation of the labeled amino acids can be achieved by various methods, such as chemical synthesis<sup>162-165</sup> or recombinant expression in an *E. coli* strain that is auxotrophic for a certain amino acid which is added into the growth medium in isotope-labeled form.<sup>166-168</sup> For example, functionally active insulin has been produced by total chemical synthesis <sup>13</sup>C=<sup>18</sup>O-labeled at a selected residue.<sup>164</sup> The synthetic method works so long as the synthesis of the whole sequence is practicable, and with the advent of the automated fast-flow peptide synthesis technology the limit of the number of amino acids in the synthetic protein has been pushed beyond 200.<sup>169,170</sup> The use of *E. coli* auxotrophs is a facile strategy as currently around 220 BL21(DE3)-based strains are available allowing production of proteins incorporating various combinations of isotopically labeled amino acids.<sup>168</sup> Native chemical ligation of synthetic or recombinantly expressed proteins is another strategy to generate relatively long protein chains incorporating isotopically labeled segments or individual amino acids; an example of a semisynthetic, segmentally isotope-labeled fully functional PLA<sub>2</sub> obtained by this method is described above (section 3.3). FTIR analysis of the lens protein  $\gamma$ D-crystallin that was produced by thioester/cysteine chemical ligation of the unlabeled N-terminal domain with the <sup>13</sup>C-labeled C-terminal domain allowed elucidation of the molecular mechanism of fibril formation.<sup>171</sup> Transmembrane proteins, such as the cation-specific ion channel p7 of hepatitis C virus (63 amino acid residues), have been produced by thioester/cysteine or hydrazide-based chemical ligation of the p7(1-26) and p7(27-63) chains that were selectively labeled with <sup>13</sup>C or <sup>15</sup>N for FTIR and NMR studies.<sup>172,173</sup> Other methods of incorporation of labeled amino acids in single or multiple sites, such as the use of modified tRNA to achieve nonsense suppression, are described below (section 6.2).

## 5.2. Local and Global Structure of A $\beta$ by Segmental Isotope Labeling

The structure of the oligomers formed by the A $\beta$ <sub>1-42</sub> peptide and its truncated/pyroglutamylated counterpart, A $\beta$ <sub>pE3-42</sub>, has been studied using synthetic peptides harboring uniformly <sup>13</sup>C, <sup>15</sup>N -labeled amino acids (Cambridge Isotope Laboratories). The labeled amino acids should constitute at least ~5-10% of the total number of residues to (a) produce a readily distinguishable amide I signal and (b) generate a normal mode vibration via inter-residue couplings that can be used for site-specific structure assessment. A $\beta$ <sub>1-42</sub> and A $\beta$ <sub>pE3-42</sub> were labeled at three or four consecutive amino acid residues, i.e. the K<sup>16</sup>L<sup>17</sup>V<sup>18</sup> or V<sup>36</sup>G<sup>37</sup>G<sup>38</sup>V<sup>39</sup> segments that play an important role in initiation of A $\beta$  aggregation<sup>174,175</sup> and were studied separately as well as combined at an equimolar ratio to gain insight into the structural pathways of fibrillogenesis. All peptide samples, incubated in aqueous buffer for 1 hour, featured a major amide I peak located





between  $1635\text{ cm}^{-1}$  and  $1630\text{ cm}^{-1}$  that constituted  $50\pm 5\%$  of the total amide I band area (Figure 10). These amide I wavenumbers indicate formation of oligomers of peptides in  $\beta$ -sheet structure with intramolecular H-bonding as the cross- $\beta$  sheet fibrils generate amide I signal below  $1630\text{ cm}^{-1}$ .<sup>50,56-58,176</sup> Smaller fractions of turn structure ( $1677\text{--}1672\text{ cm}^{-1}$ ),  $\alpha$ -helix ( $1657\text{--}1652\text{ cm}^{-1}$ ), and in some cases irregular (unordered) structure ( $\sim 1644\text{ cm}^{-1}$ ) were present as well.

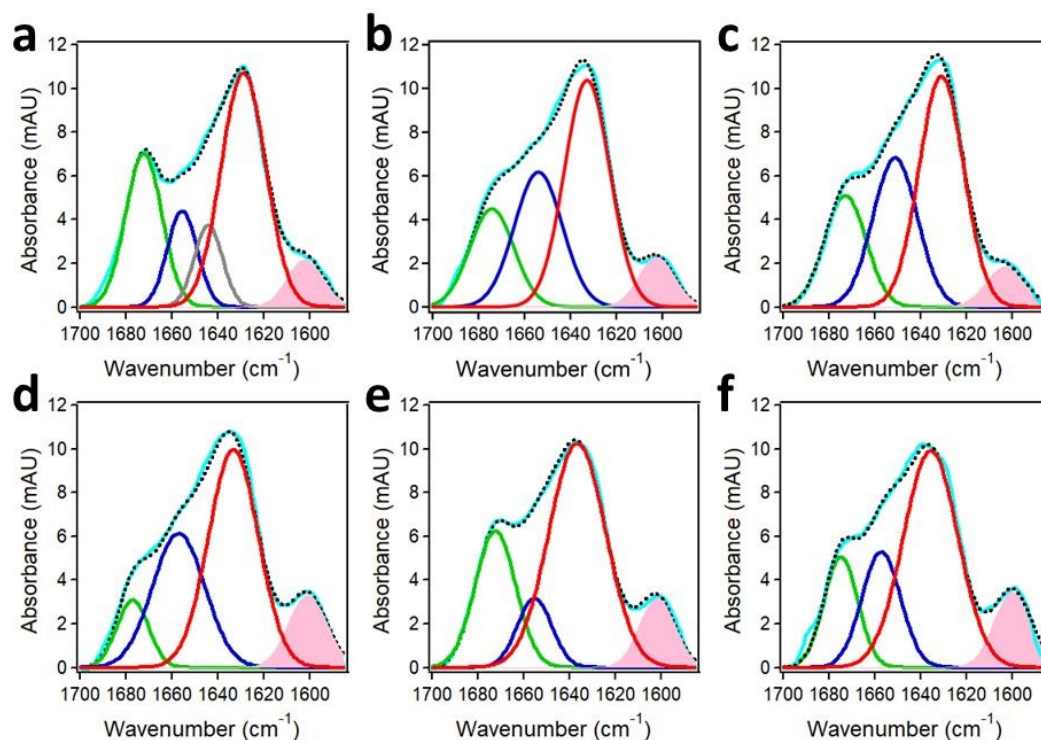


**Figure 10.** Structures of  $A\beta_{1-42}$  and  $A\beta_{3-42}$  from FTIR spectra of segmentally  $^{13}\text{C}$ ,  $^{15}\text{N}$ -labeled peptides. Peak-fitted FTIR spectra of  $\text{K}^{16}\text{L}^{17}\text{V}^{18}$ -labeled  $A\beta_{1-42}$  (a),  $\text{K}^{16}\text{L}^{17}\text{V}^{18}$ -labeled  $A\beta_{3-42}$  (b), their 1:1 combination (c),  $\text{V}^{36}\text{G}^{37}\text{G}^{38}\text{V}^{39}$ -labeled  $A\beta_{1-42}$  (d),  $\text{V}^{36}\text{G}^{37}\text{G}^{38}\text{V}^{39}$ -labeled  $A\beta_{3-42}$  (e), and their 1:1 combination (f) incubated in 50 mM NaCl + 50 mM Na,K-phosphate buffer (pD 7.2) for 1 hour. Color code: measured spectrum is cyan; the turn,  $\alpha$ -helix, irregular, and  $\beta$ -sheet components are shown in green, blue, gray, and red lines, respectively. The component generated by the  $^{13}\text{C}$ ,  $^{15}\text{N}$ -labeled segment is shaded pink. The sum of all components is shown in black dotted line. Total peptide concentration was  $50\ \mu\text{M}$ . Adapted from ref. 44, with permission.

The spectral component generated by the  $^{13}\text{C}$ ,  $^{15}\text{N}$ -labeled stretches  $\text{K}^{16}\text{L}^{17}\text{V}^{18}$  and  $\text{V}^{36}\text{G}^{37}\text{G}^{38}\text{V}^{39}$  were clearly manifested at  $1603\text{--}1602\text{ cm}^{-1}$  and  $1601\text{--}1600\text{ cm}^{-1}$  and constituted around 7% and 10% of the amide I area, respectively. These spectral features can be used to determine the mode of peptide aggregation. As indicated in section 2.2,  $^{13}\text{C}=\text{O}/^{13}\text{C}=\text{O}$  vibrational dipolar coupling, which would occur in case of in-register cross- $\beta$ -sheet formation, generates lower frequency signals ( $1594\text{--}1591\text{ cm}^{-1}$ ) whereas the  $^{13}\text{C}=\text{O}/^{12}\text{C}=\text{O}$  coupling produces signal in the  $1604\text{--}1601\text{ cm}^{-1}$  range.<sup>46,47,50,51</sup> This implies that the labeled stretches are involved in  $\beta$ -sheet structure as well, thus increasing to total  $\beta$ -sheet to around 60%. More importantly, none of the isotopically labeled segments, i.e. the 16-18 or the 36-39 stretches, are involved in coupling with labeled segments, excluding the parallel in-register  $\beta$ -sheet formation.



Instead, both peptides form  $\beta$ -hairpin-like structures upstream of residue 16 stabilized by intramolecular H-bonding. The  $\alpha$ -helix is most likely located at the N-terminus and the turn is most likely between the two  $\beta$ -strands.<sup>44</sup> The aggregation occurs via non-H-bonding interactions between these hairpin-like structures, which can exert the cytotoxic effect through various mechanisms including membrane insertion and permeabilization.<sup>151,177</sup>

## 6. CONCLUSIONS AND OUTLOOK

### 6.1. Strengths and Limitations

Isotope-edited FTIR spectroscopy offers a variety of options to analyze protein-protein and protein-membrane interactions. One of the strengths of this approach is that isotope labeling, i.e. addition of one or two neutrons in the nucleus of an atom, preserves the chemical (and most of physical) properties of the amino acid as opposed to labeling with relatively bulky exogenous molecular probes such as fluorophores or paramagnetic agents often used in fluorescence, EPR, or NMR spectroscopy. Interactions between two proteins and the accompanying conformational changes in each protein can be probed by studies on binary samples composed of an unlabeled and a uniformly  $^{13}\text{C}$  or  $^{13}\text{C},^{15}\text{N}$ -labeled protein.<sup>20,43,157,178</sup> Domain-specific, segmental, or single amino acid labeling of proteins with  $^{13}\text{C}$ ,  $^{13}\text{C},^{15}\text{N}$ , or  $^{13}\text{C}=\text{O}$  allows for amide I spectral resolution and structural characterization of the labeled site or stretch.<sup>21-23,41,162-164,166,171,179</sup> Spectral shifts in the amide II band provide an opportunity to assess the rates of the amide HX and to gain information about the solvent accessibility and the structural dynamics of the labeled and unlabeled parts of the protein. In addition, vibrational coupling effects between amide oscillators of distinct isotope content provide information on the packing of the labeled and unlabeled segments relative to each other and hence on the overall tertiary fold of the protein.<sup>44,48,49,57,58</sup> The sensitivity of the vibrational frequency to the strength of the involved covalent bonds, and consequently to the strength of H-bonding, permits distinguishing between very similar secondary structures, such as  $\alpha_{\text{I}}$ - and  $\alpha_{\text{II}}$ -helices, which is difficult to accomplish by other methods.<sup>180</sup> Polarized ATR-FTIR studies on segmentally labeled proteins reconstituted in lipid bilayers or multilayers allow determination of the orientation of the labeled segment relative to the membrane, thereby providing clues to the mode of its interaction with the membrane.<sup>106</sup>

Studies on isotope-labeled membrane lipids produce useful information on membrane structure. FTIR studies on glycerophospholipids  $^{13}\text{C}$ -labeled at *sn*-1 or *sn*-2 ester carbons yielded information on the hydration properties of the membrane surface and the orientations of the carbonyl and other chemical groups of the lipid headgroup, as well changes of these parameters during thermal phase transitions and interdigitated structure formation.<sup>72-74</sup> Data on membranes composed of selectively deuterated lipids at the *sn*-1 or *sn*-2 hydrocarbon chains can be used to determine the details of the arrangement and packing of lipids in a bilayer structure.<sup>74</sup> As shown in section 3.2, ATR-FTIR studies on supported membranes composed of an unlabeled and a chain-deuterated lipid can identify which component is preferentially hydrolyzed by  $\text{PLA}_2$ .<sup>19</sup> On the other hand, selective deuteration of one of the chains allows deciphering which reaction product (fatty acid or lyso-phospholipid) is mostly removed from the membrane upon hydrolysis by  $\text{PLA}_2$ .<sup>19</sup>

Despite these advantages, isotope-edited FTIR spectroscopy has its limitations. One inherent issue is the spectral overlap between the amide I signals generated by the unlabeled and



$^{13}\text{C}$  or  $^{13}\text{C}$ ,  $^{15}\text{N}$ -labeled chains.  $^{13}\text{C}=\text{O}$  labeling results in additional downshift of the amide I signal and thereby may offer a better spectral resolution (see section 2.2). Single amino acid labeling may be problematic for several reasons: a) technical difficulties of incorporation of a labeled amino acid in large proteins, b) too weak signal compared to the whole amide I band, and c) uncertainty regarding the secondary structure based on a local amide I mode generated by one amino acid. Solutions to (a) are described in the next section that describes nonsense suppression strategies. Even when the amide I signal of a single amino acid is reliably resolved, its spectral shift and its relation to the local secondary structure is not straightforward because the secondary structure is determined not by the frequency of an isolated amide oscillator (local mode) but by vibrational coupling with neighboring oscillators (normal mode).<sup>21,57,58</sup> The  $^{12}\text{C}/^{13}\text{C}$  vibrational coupling occurs in  $\beta$ -sheet but not in  $\alpha$ -helix conformation. Therefore, the signal generated by a single  $^{13}\text{C}$ -labeled amino acid will be diagnostic for  $\beta$ -sheet structure but cannot be used to characterize  $\alpha$ -helix structure or orientation.<sup>46,181</sup> Production of proteins isotopically labeled at single or multiple sites by the synthetic method or via nonsense suppression may present useful solutions to such problems, as discussed in the next section.

## 6.2. Future Directions

Coupling of FTIR spectroscopy with atomic force microscopy (AFM-IR) is a powerful technique that provides spatial resolution of  $\leq 10$  nm and thereby allows secondary structural analysis of protein samples or segments of distinct morphologies as opposed to the averaged FTIR spectra. Formation of prefibrillar oligomers and mature fibrils of the A $\beta$  peptide,<sup>182,183</sup>  $\alpha$ -synuclein,<sup>184</sup> or transthyretin<sup>185</sup> during the process of aggregation have been resolved by this method. Through improvements of the stability, sensitivity, and accuracy of AFM-IR, single protein molecule resolution has been achieved.<sup>186</sup> This technique has been used to analyze the response of cancer cells to drugs at single cell level and at nanoscale resolution.<sup>187</sup> Further developments in this area may involve the combination of isotope-edited protein samples with AFM-IR. For example, the molecular compositions of protein aggregates or the structural transitions in individual proteins during functional interactions can be resolved at single molecule spatial resolution.

Isotopic labeling of selected domains of proteins using techniques such as native chemical ligation represents an attractive strategy to discern domain-specific structural changes during functional turnover.<sup>171</sup> For proteins composed of disulfide bridged domains, such as the insulin receptor family proteins, the protein can be produced in unlabeled and uniformly  $^{13}\text{C}$ -labeled forms followed by disulfide reduction and re-association of the unlabeled hormone-binding  $\alpha$ -subunit with the  $^{13}\text{C}$ -labeled tyrosine-kinase  $\beta$ -subunit.<sup>188</sup> Various cell-based or cell-free expression systems for functional mammalian proteins are available that are suitable for post-translational modifications such as glycosylation. These include HEK293 cells, insect cells, wheat germ cells and cell-free systems such as rabbit reticulocyte or HeLa cell extracts,<sup>189,190</sup> which can be supplemented with isotopically labeled amino acids or labeled nutrients such as  $^{13}\text{C}_6$ -D-glucose. ATR-FTIR studies on the hormone-activation of a domain-specific isotope labeled membrane-reconstituted receptor will reveal the dynamic conformational changes in each domain reflecting the transmission of the hormone signal across the membrane. The peptide hormone itself may be produced in  $^{13}\text{C}=\text{O}$  isotopic form to move its amide I signal further away towards lower frequencies.<sup>164</sup>

Isotope labeling of one or several amino acids in a protein is crucial for obtaining site-specific structural information. A rapidly developing protein engineering strategy is the use of a



genetically modified cell or cell-free expression system containing a stop (nonsense, termination) codon in a given gene, such as TAG (amber), at the site of interest and a nonsense suppressor tRNA aminoacylated with a labeled amino acid and harboring an anticodon complementary to the stop codon (CUA, in this case).<sup>191-194</sup> The selected stop codon as well as the suppressor tRNA/amino acyl tRNA synthetase (aaRS) pair should be orthogonal (heterologous) to the host organism or the cell-free system to prevent cross-reaction. In the semisynthetic method, the tRNA<sub>CUA</sub> lacking the last two nucleotides is prepared by in vitro transcription with T7 RNA polymerase and the synthetic, labeled amino acid dinucleotide is appended to the 3' end with the T4 RNA ligase.<sup>192,195</sup> A similar method uses flexible tRNA acylation ribozymes coupled with a translation system containing the activated, labeled or otherwise modified amino acid.<sup>196,197</sup> More than one labeled amino acids can be incorporated in a protein by using other stop codons such as TAA (ochre) or TGA (opal) coupled with respective suppressor tRNAs, i.e. tRNA<sub>UUA</sub> or tRNA<sub>UCA</sub> provided the expression system is using a third stop codon.<sup>198,199</sup> Artificial, such as quadruplet codons can be introduced alone or in tandem with an orthogonal stop codon resulting in double nonsense/frameshift suppression and incorporation of two labeled or unnatural amino acids allowing for simultaneous targeting of two sites in a protein.<sup>191,193,200</sup> Three or four noncanonical amino acids have been incorporated in one protein chain by using all three natural stop codons<sup>194</sup> or by engineering four suppressor tRNA/aaRS pairs targeting four frameshift quadruplet codons.<sup>201</sup> Future efforts will likely expand the scope of protein engineering allowing facile production of proteins labeled at multiple sites through orthogonal tRNA/aaRS pairs or chemically aminoacylated tRNAs that work efficiently in mammalian expression systems, which will enhance the ability of isotope-edited FTIR spectroscopy to gain higher resolution structural insight into the function of important proteins.

## Conflict of Interest

The author declares no conflict of interest.

## Data Availability

No primary research results, software or code have been included and no new data were generated or analyzed as part of this review.

## Acknowledgments

This work has been supported, in part, by Florida Department of Health, Ed and Ethel Moore Alzheimer's Disease Research Program (grant 21A06).

## REFERENCES

1. Corbi-Verge C, Kim PM. Motif mediated protein-protein interactions as drug targets. *Cell Commun Signal*. 2016 Mar 2;14:8.
2. Sluchanko NN, Bustos DM. Intrinsic disorder associated with 14-3-3 proteins and their partners. *Prog Mol Biol Transl Sci*. 2019;166:19-61.



- Kapingidza AB, Kowal K, Chruszcz M. Antigen-Antibody Complexes. *Subcell Biochem.* 2020;94:465-497.
- Scott DE, Bayly AR, Abell C, Skidmore J. (2016) Small molecules, big targets: drug discovery faces the protein-protein interaction challenge. *Nat Rev Drug Discov.* 15(8), 533–550.
- Wu D, Li Y, Zheng L, Xiao H, Ouyang L, Wang G, Sun Q. Small molecules targeting protein-protein interactions for cancer therapy. *Acta Pharm Sin B.* 2023 Oct;13(10):4060-4088.
- Murabito A, Bhatt J, Ghigo A. It Takes Two to Tango! Protein-Protein Interactions behind cAMP-Mediated CFTR Regulation. *Int J Mol Sci.* 2023 Jun 23;24(13):10538.
- Overduin M, Kervin TA. The phosphoinositide code is read by a plethora of protein domains. *Expert Rev Proteomics.* 2021 Jul;18(7):483-502.
- Overduin M, Kervin TA, Klarenbach Z, Adra TRC, Bhat RK. Comprehensive classification of proteins based on structures that engage lipids by COMPOSEL. *Biophys Chem.* 2023 Apr;295:106971.
- Tubiana T, Sillitoe I, Orengo C, Reuter N. Dissecting peripheral protein-membrane interfaces. *PLoS Comput Biol.* 2022 Dec 14;18(12):e1010346.
- Guaita M, Watters SC, Loerch S. Recent advances and current trends in cryo-electron microscopy. *Curr Opin Struct Biol.* 2022 Dec;77:102484.
- Berger C, Premaraj N, Ravelli RBG, Knoop K, López-Iglesias C, Peters PJ. Cryo-electron tomography on focused ion beam lamellae transforms structural cell biology. *Nat Methods.* 2023 Apr;20(4):499-511.
- Viles JH. Imaging amyloid- $\beta$  membrane interactions: Ion-channel pores and lipid-bilayer permeability in Alzheimer's disease. *Angew. Chem. Int. Ed. Engl.* 62(25), e202215785 (2023).
- Irvin EM, Wang H. Single-molecule imaging of genome maintenance proteins encountering specific DNA sequences and structures. *DNA Repair (Amst).* 2023 Aug;128:103528.
- Deopa SPS, Patil S. Viscoelasticity of single folded proteins using dynamic atomic force microscopy. *Soft Matter.* 2023 Jun 14;19(23):4188-4203.
- Müller DJ, Dumitru AC, Lo Giudice C, Gaub HE, Hinterdorfer P, Hummer G, De Yoreo JJ, Dufrène YF, Alsteens D. Atomic Force Microscopy-Based Force Spectroscopy and Multiparametric Imaging of Biomolecular and Cellular Systems. *Chem Rev.* 2021 Oct 13;121(19):11701-11725.
- Flehsig H, Ando T. Protein dynamics by the combination of high-speed AFM and computational modeling. *Curr Opin Struct Biol.* 2023 Jun;80:102591.
- Pinchas S, Laulicht I. *Infrared Spectra of Labeled Compounds.* Academic Press, London and New York, 1971.
- Tatulian SA. FTIR Analysis of Proteins and Protein-Membrane Interactions. *Methods Mol Biol.* 2019;2003:281-325.
- Tatulian SA. Toward understanding interfacial activation of secretory phospholipase A2 (PLA2): membrane surface properties and membrane-induced structural changes in the enzyme contribute synergistically to PLA2 activation. *Biophys J.* 2001 Feb;80(2):789-800.
- Haris PI. Probing protein-protein interaction in biomembranes using Fourier transform infrared spectroscopy. *Biochim Biophys Acta.* 2013 Oct;1828(10):2265-71.
- Decatur SM. Elucidation of residue-level structure and dynamics of polypeptides via isotope-edited infrared spectroscopy. *Acc Chem Res.* 2006 Mar;39(3):169-75.



22. Arkin IT. Isotope-edited IR spectroscopy for the study of membrane proteins. *Curr Opin Chem Biol.* 2006 Oct;10(5):394-401.
23. Manor J, Arkin IT. Gaining insight into membrane protein structure using isotope-edited FTIR. *Biochim Biophys Acta.* 2013 Oct;1828(10):2256-64.
24. MacPhail RA, Strauss HL, Snyder RG, Elliger CA. C-H Stretching Modes and the Structure of n-Alkyl Chains. 2. Long, All-Trans Chains. *J. Phys. Chem.* 1984, 88:334-341.
25. Kodati VR, El-Jastimi R, Lafleur M. Contribution of the Intermolecular Coupling and Librotorsional Mobility in the Methylene Stretching Modes in the Infrared Spectra of Acyl Chains. *J Phys Chem.* 1994, 98:12191-12197.
26. Snyder RG, Hsu SL, Krimm S. Vibrational spectra in the C-H stretching region and the structure of the polymethylene chain. *Spectrochimica Acta.* 1978. 34A:395-406.
27. Tadesse L, Nazarbaghi R, Walters L. Isotopically Enhanced Infrared Spectroscopy: A Novel Method for Examining Secondary Structure at Specific Sites in Conformationally Heterogeneous Peptides. *J. Am. Chem. Soc.* 1991, 113:7036-7037.
28. Silva RA, Kubelka J, Bour P, Decatur SM, Keiderling TA. Site-specific conformational determination in thermal unfolding studies of helical peptides using vibrational circular dichroism with isotopic substitution. *Proc Natl Acad Sci U S A.* 2000 Jul 18;97(15):8318-23.
29. Brauner JW, Dugan C, Mendelsohn R. <sup>13</sup>C Isotope Labeling of Hydrophobic Peptides. Origin of the Anomalous Intensity Distribution in the Infrared Amide I Spectral Region of  $\beta$ -Sheet Structures. *J Am Chem Soc.* 2000, 122:677-683.
30. Venyaminov SY, Hedstrom JF, Prendergast FG. Analysis of the segmental stability of helical peptides by isotope-edited infrared spectroscopy. *Proteins.* 2001 Oct 1;45(1):81-9.
31. Pastrana-Rios B. Mechanism of unfolding of a model helical peptide. *Biochemistry.* 2001 Aug 7;40(31):9074-81.
32. Huang CY, Getahun Z, Zhu Y, Klemke JW, DeGrado WF, Gai F. Helix formation via conformation diffusion search. *Proc Natl Acad Sci USA.* 2002 99(5):2788-93.
33. Huang R, Kubelka J, Barber-Armstrong W, Silva RA, Decatur SM, Keiderling TA. Nature of vibrational coupling in helical peptides: an isotopic labeling study. *Journal of the American Chemical Society.* 2004 Mar 3;126(8):2346-54.
34. Barber-Armstrong W, Donaldson T, Wijesooriya H, Silva RA, Decatur SM. Empirical relationships between isotope-edited IR spectra and helix geometry in model peptides. *J Am Chem Soc.* 2004 Mar 3;126(8):2339-45.
35. Decatur SM. IR spectroscopy of isotope-labeled helical peptides: probing the effect of N-acetylation on helix stability. *Biopolymers.* 2000 Sep;54(3):180-5.
36. Bouř P, Keiderling TA. Ab initio modeling of amide I coupling in antiparallel beta-sheets and the effect of <sup>13</sup>C isotopic labeling on infrared spectra. *J Phys Chem B.* 2005 Mar 24;109(11):5348-57.
37. Goldblatt G, Cilenti L, Matos JO, Lee B, Ciaffone N, Wang QX, Tetard L, Teter K, Tatulian SA. Unmodified and pyroglutamylated amyloid  $\beta$  peptides form hypertoxic hetero-oligomers of unique secondary structure. *FEBS J.* 2017 May;284(9):1355-1369.
38. Arkin IT, MacKenzie KR, Brünger AT. Site-directed dichroism as a method for obtaining rotational and orientational constraints for oriented polymers. *J Am Chem Soc.* 1997, 119(38):8973-80.



39. Das KP, Choo-Smith LP, Petrash JM, Surewicz WK. Insight into the secondary structure of non-native proteins bound to a molecular chaperone alpha-crystallin. An isotope-edited infrared spectroscopic study. *J Biol Chem.* 1999 Nov 19;274(47):33209-12.
40. Torres J, Kukol A, Goodman JM, Arkin IT. Site-specific examination of secondary structure and orientation determination in membrane proteins: the peptidic (13)C=(18)O group as a novel infrared probe. *Biopolymers.* 2001 Nov;59(6):396-401.
41. Baronio CM, Baldassarre M, Barth A. Insight into the internal structure of amyloid- $\beta$  oligomers by isotope-edited Fourier transform infrared spectroscopy. *Phys Chem Chem Phys.* 2019 Apr 17;21(16):8587-8597.
42. Haris PI, Robillard GT, van Dijk AA, Chapman D. Potential of  $^{13}\text{C}$  and  $^{15}\text{N}$  labeling for studying protein-protein interactions using Fourier transform infrared spectroscopy. *Biochemistry.* 1992 Jul 14;31(27):6279-84.
43. Zhang M, Fabian H, Mantsch HH, Vogel HJ. Isotope-edited Fourier transform infrared spectroscopy studies of calmodulin's interaction with its target peptides. *Biochemistry.* 1994 Sep 13;33(36):10883-8.
44. Goldblatt G, Matos JO, Gornto J, Tatulian SA. Isotope-edited FTIR reveals distinct aggregation and structural behaviors of unmodified and pyroglutamylated amyloid  $\beta$  peptides. *Phys Chem Chem Phys.* 2015 Dec 28;17(48):32149-60.
45. Tatulian SA, Tamm LK. Secondary structure, orientation, oligomerization, and lipid interactions of the transmembrane domain of influenza hemagglutinin. *Biochemistry.* 2000 Jan 25;39(3):496-507.
46. Paul C, Wang J, Wimley WC, Hochstrasser RM, Axelsen PH. Vibrational coupling, isotopic editing, and beta-sheet structure in a membrane-bound polypeptide. *J Am Chem Soc.* 2004 May 12;126(18):5843-50.
47. Petty SA, Decatur SM. Experimental evidence for the reorganization of beta-strands within aggregates of the A $\beta$ (16-22) peptide. *J Am Chem Soc.* 2005 Oct 5;127(39):13488-9.
48. Huang R, Setnička V, Etienne MA, Kim J, Kubelka J, Hammer RP, Keiderling TA. Cross-Strand Coupling of a  $\beta$ -Hairpin Peptide Stabilized with an Aib-Gly Turn Studied Using Isotope-Edited IR Spectroscopy. *J Am Chem Soc.* 2007 129 (44):13592-13603.
49. Scheerer D, Chi H, McElheny D, Keiderling TA, Hauser K. Enhanced Sensitivity to Local Dynamics in Peptides by Use of Temperature-Jump IR Spectroscopy and Isotope Labeling. *Chemistry.* 2020 Mar 18;26(16):3524-3534.
50. Paul C, Axelsen PH. beta Sheet structure in amyloid beta fibrils and vibrational dipolar coupling. *J Am Chem Soc.* 2005 Apr 27;127(16):5754-5.
51. Petty SA, Decatur SM. Intersheet rearrangement of polypeptides during nucleation of {beta}-sheet aggregates. *Proc Natl Acad Sci U S A.* 2005 Oct 4;102(40):14272-7.
52. Kukol A, Torres J, Arkin IT. A structure for the trimeric MHC class II-associated invariant chain transmembrane domain. *J Mol Biol.* 2002 Jul 26;320(5):1109-17.
53. Beevers AJ, Kukol A. The transmembrane domain of the oncogenic mutant ErbB-2 receptor: a structure obtained from site-specific infrared dichroism and molecular dynamics. *J Mol Biol.* 2006 Sep 1;361(5):945-53.
54. Arbely E, Kass I, Arkin IT. Site-specific dichroism analysis utilizing transmission FTIR. *Biophys J.* 2003 Oct;85(4):2476-83.



55. Remorino A, Korendovych IV, Wu Y, DeGrado WF, Hochstrasser RM. Residue-specific vibrational echoes yield 3D structures of a transmembrane helix dimer. *Science*. 2011 Jun 3;332(6034):1206-9.
56. Kim YS, Liu L, Axelsen PH, Hochstrasser RM. Two-dimensional infrared spectra of isotopically diluted amyloid fibrils from A $\beta$ 40. *Proc Natl Acad Sci U S A*. 2008 Jun 3;105(22):7720-5.
57. Moran SD, Zanni MT. How to Get Insight into Amyloid Structure and Formation from Infrared Spectroscopy. *J Phys Chem Lett*. 2014 Jun 5;5(11):1984-1993.
58. Maj M, Lomont JP, Rich KL, Alperstein AM, Zanni MT. Site-specific detection of protein secondary structure using 2D IR dihedral indexing: a proposed assembly mechanism of oligomeric hIAPP. *Chem Sci*. 2018, 9(2):463-474.
59. Rodríguez-Pérez JC, Hamley IW, Gras SL, Squires AM. Local orientational disorder in peptide fibrils probed by a combination of residue-specific  $^{13}\text{C}$ - $^{18}\text{O}$  labelling, polarised infrared spectroscopy and molecular combing. *Chem Commun (Camb)*. 2012 Dec 18;48(97):11835-7.
60. Rana FR, Mautone AJ, Dluhy RA. Combined Infrared and  $^{31}\text{P}$  NMR Spectroscopic Method for Determining the Fractional Composition in Langmuir-Blodgett Films of Binary Phospholipid Mixtures. *Applied Spectroscopy* 1993, 47(7):1015-1023.
61. Reinl HM, Bayerl TM. Lipid transfer between small unilamellar vesicles and single bilayers on a solid support: self-assembly of supported bilayers with asymmetric lipid distribution. *Biochemistry*. 1994 Nov 29;33(47):14091-9.
62. Dibble AR, Hinderliter AK, Sando JJ, Biltonen RL. Lipid lateral heterogeneity in phosphatidylcholine/phosphatidylserine/diacylglycerol vesicles and its influence on protein kinase C activation. *Biophys J*. 1996 Oct;71(4):1877-90.
63. Lasch P, Schultz CP, Naumann D. The influence of poly-(L-lysine) and porin on the domain structure of mixed vesicles composed of lipopolysaccharide and phospholipid: an infrared spectroscopic study. *Biophys J*. 1998 Aug;75(2):840-52.
64. Brockman JM, Wang Z, Notter RH, Dluhy RA. Effect of hydrophobic surfactant proteins SP-B and SP-C on binary phospholipid monolayers: II. Infrared external reflectance-absorption spectroscopy. *Biophys J*. 2003 Jan;84(1):326-40.
65. Dluhy RA, Moffatt D, Cameron DG, Mendelsohn R, Mantsch HH. Characterization of cooperative conformational transitions by Fourier transform infrared spectroscopy: application to phospholipid binary mixtures. *Can. J. Chem*. 1985, 63:1925-1932.
66. Moore DJ, Sills RH, Patel N, Mendelsohn R. Conformational order of phospholipids incorporated into human erythrocytes: an FTIR spectroscopy study. *Biochemistry*. 1996 Jan 9;35(1):229-35.
67. Casal HL, Mantsch HH. Polymorphic phase behaviour of phospholipid membranes studied by infrared spectroscopy. *Biochim Biophys Acta*. 1984 Dec 4;779(4):381-401.
68. Villalaín J, Gómez-Fernández JC. Fourier transform infrared spectroscopic study of mixtures of palmitic acid with dipalmitoylphosphatidylcholine using isotopic substitution. *Chem Phys Lipids*. 1992, 62:19-29.
69. López-García F, Villalaín J, Gómez-Fernández JC, Quinn PJ. The phase behavior of mixed aqueous dispersions of dipalmitoyl derivatives of phosphatidylcholine and diacylglycerol. *Biophys J*. 1994 Jun;66(6):1991-2004.





70. Mendelsohn R, Davies MA, Brauner JW, Schuster HF, Dluhy RA. Quantitative determination of conformational disorder in the acyl chains of phospholipid bilayers by infrared spectroscopy. *Biochemistry*. 1989 Oct 31;28(22):8934-9.
71. Mendelsohn R, Liang GL, Strauss HL, Snyder RG. IR spectroscopic determination of gel state miscibility in long-chain phosphatidylcholine mixtures. *Biophys J*. 1995 Nov;69(5):1987-98.
72. Blume A, Hübner W, Messner G. Fourier transform infrared spectroscopy of  $^{13}\text{C} = \text{O}$ -labeled phospholipids hydrogen bonding to carbonyl groups. *Biochemistry*. 1988 Oct 18;27(21):8239-49.
73. Hübner W, Mantsch HH. Orientation of specifically  $^{13}\text{C} = \text{O}$  labeled phosphatidylcholine multilayers from polarized attenuated total reflection FT-IR spectroscopy. *Biophys J*. 1991 Jun;59(6):1261-72.
74. Lewis RN, McElhaney RN. Studies of mixed-chain diacyl phosphatidylcholines with highly asymmetric acyl chains: a Fourier transform infrared spectroscopic study of interfacial hydration and hydrocarbon chain packing in the mixed interdigitated gel phase. *Biophys J*. 1993 Nov;65(5):1866-77.
75. Lewis RN, McElhaney RN, Pohle W, Mantsch HH. Components of the carbonyl stretching band in the infrared spectra of hydrated 1,2-diacylglycerolipid bilayers: a reevaluation. *Biophys J*. 1994 Dec;67(6):2367-75.
76. Villalain J, Gomez-Fernandez JC. FT-IR study of the hydrogen bonding interaction between cholesterol and DPPC. *Biochem Soc Trans*. 1992 May;20(2):122S.
77. Pande AH, Moe D, Nemecek KN, Qin S, Tan S, Tatulian SA. Modulation of human 5-lipoxygenase activity by membrane lipids. *Biochemistry*. 2004 Nov 23;43(46):14653-66.
78. Tatulian SA. Structural effects of covalent inhibition of phospholipase A2 suggest allosteric coupling between membrane binding and catalytic sites. *Biophys J*. 2003 Mar;84(3):1773-83.
79. Allen KN, Entova S, Ray LC, Imperiali B. Monotopic Membrane Proteins Join the Fold. *Trends Biochem Sci*. 2019 Jan;44(1):7-20.
80. Boulos I, Jabbour J, Khoury S, Mikhael N, Tishkova V, Candoni N, Ghadieh HE, Veessler S, Bassim Y, Azar S, Harb F. Exploring the World of Membrane Proteins: Techniques and Methods for Understanding Structure, Function, and Dynamics. *Molecules*. 2023 Oct 19;28(20):7176.
81. Li B, Mendenhall J, Meiler J. Interfaces Between Alpha-helical Integral Membrane Proteins: Characterization, Prediction, and Docking. *Comput Struct Biotechnol J*. 2019 May 25;17:699-711.
82. Marinko JT, Huang H, Penn WD, Capra JA, Schleich JP, Sanders CR. Folding and Misfolding of Human Membrane Proteins in Health and Disease: From Single Molecules to Cellular Proteostasis. *Chem Rev*. 2019 May 8;119(9):5537-5606.
83. Mayse LA, Movileanu L. Gating of  $\beta$ -Barrel Protein Pores, Porins, and Channels: An Old Problem with New Facets. *Int J Mol Sci*. 2023 Jul 28;24(15):12095.
84. Chiu YC, Yeh MC, Wang CH, Chen YA, Chang H, Lin HY, Ho MC, Lin SM. Structural basis for calcium-stimulating pore formation of *Vibrio*  $\alpha$ -hemolysin. *Nat Commun*. 2023 Sep 23;14(1):5946.
85. Fhu CW, Ali A. Protein Lipidation by Palmitoylation and Myristoylation in Cancer. *Front Cell Dev Biol*. 2021 May 20;9:673647.



86. Shang S, Liu J, Hua F. Protein acylation: mechanisms, biological functions and therapeutic targets. *Signal Transduct Target Ther.* 2022 Dec 29;7(1):396.
87. Dennis KMJH, Heather LC. Post-translational palmitoylation of metabolic proteins. *Front Physiol.* 2023 Feb 24;14:1122895.
88. Müller GA, Müller TD. (Patho)Physiology of Glycosylphosphatidylinositol-Anchored Proteins I: Localization at Plasma Membranes and Extracellular Compartments. *Biomolecules.* 2023 May 18;13(5):855.
89. Müller GA, Müller TD. (Patho)Physiology of Glycosylphosphatidylinositol-Anchored Proteins II: Intercellular Transfer of Matter (Inheritance?) That Matters. *Biomolecules.* 2023 Jun 15;13(6):994.
90. Jung D, Bachmann HS. Regulation of protein prenylation. *Biomed Pharmacother.* 2023 Aug;164:114915.
91. Villanueva CE, Hagenbuch B. Palmitoylation of solute carriers. *Biochem Pharmacol.* 2023 Sep;215:115695.
92. Fuglebakk E, Reuter N. A model for hydrophobic protrusions on peripheral membrane proteins. *PLoS Comput Biol.* 2018 Jul 26;14(7):e1006325.
93. Pemberton JG, Balla T. Polyphosphoinositide-Binding Domains: Insights from Peripheral Membrane and Lipid-Transfer Proteins. *Adv Exp Med Biol.* 2019;1111:77-137.
94. Tatulian SA. Interfacial Enzymes: Membrane Binding, Orientation, Membrane Insertion, and Activity. *Methods Enzymol.* 2017;583:197-230.
95. Muller MP, Jiang T, Sun C, Lihan M, Pant S, Mahinthichaichan P, Trifan A, Tajkhorshid E. Characterization of Lipid-Protein Interactions and Lipid-Mediated Modulation of Membrane Protein Function through Molecular Simulation. *Chem Rev.* 2019 May 8;119(9):6086-6161.
96. Ray S, Scott JL, Tatulian SA. Effects of lipid phase transition and membrane surface charge on the interfacial activation of phospholipase A2. *Biochemistry.* 2007 Nov 13;46(45):13089-100.
97. Speijer H, Giesen PL, Zwaal RF, Hack CE, Hermens WT. Critical micelle concentrations and stirring are rate limiting in the loss of lipid mass during membrane degradation by phospholipase A2. *Biophys J.* 1996 May;70(5):2239-47.
98. Callisen TH, Talmon Y. Direct imaging by cryo-TEM shows membrane break-up by phospholipase A2 enzymatic activity. *Biochemistry.* 1998 Aug 4;37(31):10987-93.
99. Vacklin HP, Tiberg F, Fragneto G, Thomas RK. Phospholipase A2 hydrolysis of supported phospholipid bilayers: a neutron reflectivity and ellipsometry study. *Biochemistry.* 2005 Mar 1;44(8):2811-21.
100. Jain MK, Rogers J, Jahagirdar DV, Marecek JF, Ramirez F. Kinetics of interfacial catalysis by phospholipase A2 in intravesicle scooting mode, and heterofusion of anionic and zwitterionic vesicles. *Biochim Biophys Acta.* 1986 Sep 11;860(3):435-47.
101. Bayburt T, Yu BZ, Lin HK, Browning J, Jain MK, Gelb MH. Human nonpancreatic secreted phospholipase A2: interfacial parameters, substrate specificities, and competitive inhibitors. *Biochemistry.* 1993 Jan 19;32(2):573-82.
102. Burack WR, Biltonen RL. Lipid bilayer heterogeneities and modulation of phospholipase A2 activity. *Chem Phys Lipids.* 1994 Sep 6;73(1-2):209-22.
103. Burack WR, Dibble AR, Allietta MM, Biltonen RL. Changes in vesicle morphology induced by lateral phase separation modulate phospholipase A2 activity. *Biochemistry.* 1997 Aug 26;36(34):10551-7.



104. Pande AH, Qin S, Nemecek KN, He X, Tatulian SA. Isoform-specific membrane insertion of secretory phospholipase A2 and functional implications. *Biochemistry*. 2006 Oct 17;45(41):12436-47.
105. Tatulian SA. Attenuated total reflection Fourier transform infrared spectroscopy: a method of choice for studying membrane proteins and lipids. *Biochemistry*. 2003 Oct 21;42(41):11898-907.
106. Tatulian SA, Qin S, Pande AH, He X. Positioning membrane proteins by novel protein engineering and biophysical approaches. *J Mol Biol*. 2005 Sep 2;351(5):939-47.
107. Yu, B. Z., Janssen, M. J.W., Verheij, H. M. & Jain, M. K. (2000). Control of the chemical step by leucine-31 of pancreatic phospholipase A2. *Biochemistry*, 39, 5702–5711.
108. Berg, O. G., Gelb, M. H., Tsai, M. D. & Jain, M. K. (2001). Interfacial enzymology: the secreted phospholipase A2-paradigm. *Chem. Rev.* 101, 2613–2654.
109. Keskin O, Gursoy A, Ma B, Nussinov R. Principles of protein-protein interactions: what are the preferred ways for proteins to interact? *Chem Rev*. 2008 Apr;108(4):1225-44.
110. Perkins JR, Diboun I, Dessailly BH, Lees JG, Orengo C. Transient protein-protein interactions: structural, functional, and network properties. *Structure*. 2010 Oct 13;18(10):1233-43.
111. Akiba H, Tsumoto K. Thermodynamics of antibody-antigen interaction revealed by mutation analysis of antibody variable regions. *J Biochem*. 2015 Jul;158(1):1-13.
112. Tatulian SA. INSR. In: *Encyclopedia of Signaling Molecules*, 2<sup>nd</sup> Edition, Choi S, ed., Springer, p. 2608-2619, 2018.
113. Oldfield CJ, Meng J, Yang JY, Yang MQ, Uversky VN, Dunker AK. Flexible nets: disorder and induced fit in the associations of p53 and 14-3-3 with their partners. *BMC Genomics*. 2008;9 Suppl 1(Suppl 1):S1.
114. Xu Y, Kong GK, Menting JG, Margetts MB, Delaine CA, Jenkin LM, Kiselyov VV, De Meyts P, Forbes BE, Lawrence MC. How ligand binds to the type 1 insulin-like growth factor receptor. *Nat Commun*. 2018 Feb 26;9(1):821.
115. Kaur H, Salunke DM. Antibody promiscuity: Understanding the paradigm shift in antigen recognition. *IUBMB Life*. 2015 Jul;67(7):498-505.
116. Arai M, Suetaka S, Ooka K. Dynamics and interactions of intrinsically disordered proteins. *Curr Opin Struct Biol*. 2023 Nov 30;84:102734.
117. Hennig O, Philipp S, Bonin S, Rollet K, Kolberg T, Jühling T, Betat H, Sauter C, Mörl M. Adaptation of the *Romanomermis culicivorax* CCA-Adding Enzyme to Miniaturized Armless tRNA Substrates. *Int J Mol Sci*. 2020 Nov 28;21(23):9047.
118. Gattkowsky E, Rutherford TJ, Möckl F, Bauche A, Sander S, Flieger R, Tidow H. Analysis of ligand binding and resulting conformational changes in pyrophosphatase NUDT9. *FEBS J*. 2021 Dec;288(23):6769-6782.
119. Su D, Kosciuk T, Yang M, Price IR, Lin H. Binding Affinity Determines Substrate Specificity and Enables Discovery of Substrates for N-Myristoyltransferases. *ACS Catal*. 2021 Dec 17;11(24):14877-14883.
120. Hager M, Pöhler MT, Reinhardt F, Wellner K, Hübner J, Betat H, Prohaska S, Mörl M. Substrate Affinity Versus Catalytic Efficiency: Ancestral Sequence Reconstruction of tRNA Nucleotidyltransferases Solves an Enzyme Puzzle. *Mol Biol Evol*. 2022 Dec 5;39(12):msac250.
121. Moreno-Córdova EN, Arvizu-Flores AA, Valenzuela-Soto EM, García-Orozco KD, Wall-Medrano A, Alvarez-Parrilla E, Ayala-Zavala JF, Domínguez-Avila JA, González-Aguilar



- GA. Gallotannins are uncompetitive inhibitors of pancreatic lipase activity. *Biophys Chem.* 2020 Sep;264:106409.
122. Dacol EC, Wang S, Chen Y, Lepique AP. The interaction of SET and protein phosphatase 2A as target for cancer therapy. *Biochim Biophys Acta Rev Cancer.* 2021 Aug;1876(1):188578.
123. Mitchell RA, Luwor RB, Burgess AW. Epidermal growth factor receptor: Structure-function informing the design of anticancer therapeutics. *Exp Cell Res.* 2018 Oct 1;371(1):1-19.
124. Hoffmann MM, Slansky JE. T-cell receptor affinity in the age of cancer immunotherapy. *Mol Carcinog.* 2020 Jul;59(7):862-870.
125. Zheng S, Zou M, Shao Y, Wu H, Wu H, Wang X. Two-dimensional measurements of receptor-ligand interactions. *Front Mol Biosci.* 2023 Feb 17;10:1154074.
126. Midelfort KS, Witttrup KD. Context-dependent mutations predominate in an engineered high-affinity single chain antibody fragment. *Protein Sci.* 2006 Feb;15(2):324-34.
127. Diop A, Santorelli D, Malagrino F, Nardella C, Pennacchiotti V, Pagano L, Marcocci L, Pietrangeli P, Gianni S, Toto A. SH2 Domains: Folding, Binding and Therapeutical Approaches. *Int J Mol Sci.* 2022 Dec 15;23(24):15944.
128. Amacher JF, Brooks L, Hampton TH, Madden DR. Specificity in PDZ-peptide interaction networks: Computational analysis and review. *J Struct Biol X.* 2020;4:100022.
129. Thurairajah B, Hudson AJ, Doveston RG. Contemporary biophysical approaches for studying 14-3-3 protein-protein interactions. *Front Mol Biosci.* 2022 Nov 8;9:1043673.
130. Shah NH, Amacher JF, Nocka LM, Kuriyan J. The Src module: an ancient scaffold in the evolution of cytoplasmic tyrosine kinases. *Crit Rev Biochem Mol Biol.* 2018 Oct;53(5):535-563.
131. Abhishek S, Deeksha W, Nethravathi KR, Davari MD, Rajakumara E. Allosteric crosstalk in modular proteins: Function fine-tuning and drug design. *Comput Struct Biotechnol J.* 2023 Oct 10;21:5003-5015.
132. Akter R, Cao P, Noor H, Ridgway Z, Tu LH, Wang H, Wong AG, Zhang X, Abedini A, Schmidt AM, Raleigh DP. Islet Amyloid Polypeptide: Structure, Function, and Pathophysiology. *J Diabetes Res.* 2016;2016:2798269.
133. Yuzu K, Lindgren M, Nyström S, Zhang J, Mori W, Kunitomi R, Nagase T, Iwaya K, Hammarström P, Zako T. Insulin amyloid polymorphs: implications for iatrogenic cytotoxicity. *RSC Adv.* 2020 Oct 12;10(62):37721-37727.
134. Liz MA, Coelho T, Bellotti V, Fernandez-Arias MI, Mallaina P, Obici L. A Narrative Review of the Role of Transthyretin in Health and Disease. *Neurol Ther.* 2020 Dec;9(2):395-402.
135. Maity D, Pal D. Molecular Dynamics of Hemoglobin Reveals Structural Alterations and Explains the Interactions Driving Sick Cell Fibrillation. *J Phys Chem B.* 2021 Sep 9;125(35):9921-9933.
136. Nguyen PH, Ramamoorthy A, Sahoo BR, Zheng J, Faller P, Straub JE, Dominguez L, Shea JE, Dokholyan NV, De Simone A, Ma B, Nussinov R, Najafi S, Ngo ST, Loquet A, Chiricotto M, Ganguly P, McCarty J, Li MS, Hall C, Wang Y, Miller Y, Melchionna S, Habenstein B, Timr S, Chen J, Hnath B, Strodel B, Kayed R, Lesné S, Wei G, Sterpone F, Doig AJ, Derreumaux P. Amyloid Oligomers: A Joint Experimental/Computational Perspective on Alzheimer's Disease, Parkinson's Disease, Type II Diabetes, and Amyotrophic Lateral Sclerosis. *Chem Rev.* 2021 Feb 24;121(4):2545-2647.



137. Buxbaum JN, Dispenzieri A, Eisenberg DS, Fändrich M, Merlini G, Saraiva MJM, Sekijima Y, Westermark P. Amyloid nomenclature 2022: update, novel proteins, and recommendations by the International Society of Amyloidosis (ISA) Nomenclature Committee. *Amyloid*. 2022 Dec;29(4):213-219.
138. Kulichikhin KY, Malikova OA, Zobnina AE, Zalutskaya NM, Rubel AA. Interaction of Proteins Involved in Neuronal Proteinopathies. *Life (Basel)*. 2023 Sep 23;13(10):1954.
139. Starr N, Ioannou A, Martinez-Naharro A. Monitoring cardiac amyloidosis with multimodality imaging. *Rev Esp Cardiol (Engl Ed)*. 2023 Sep 9:S1885-5857(23)00237-2.
140. Louros N, Schymkowitz J, Rousseau F. Mechanisms and pathology of protein misfolding and aggregation. *Nat Rev Mol Cell Biol*. 2023 Sep 8.
141. Al Adem K, Lee S. Structural polymorphism and cytotoxicity of brain-derived  $\beta$ -amyloid extracts. *Protein Sci*. 2023 May;32(5):e4639.
142. Swamy KBS, Schuyler SC, Leu JY. Protein Complexes Form a Basis for Complex Hybrid Incompatibility. *Front Genet*. 2021 Feb 9;12:609766.
143. Kanitkar TR, Sen N, Nair S, Soni N, Amritkar K, Ramtirtha Y, Madhusudhan MS. Methods for Molecular Modelling of Protein Complexes. *Methods Mol Biol*. 2021;2305:53-80.
144. Piersimoni L, Kastritis PL, Arlt C, Sinz A. Cross-Linking Mass Spectrometry for Investigating Protein Conformations and Protein-Protein Interactions—A Method for All Seasons. *Chem Rev*. 2022 Apr 27;122(8):7500-7531.
145. Couée I, Gouesbet G. Protein-Protein Interactions in Abiotic Stress Signaling: An Overview of Biochemical and Biophysical Methods of Characterization. *Methods Mol Biol*. 2023;2642:319-330.
146. O'Reilly FJ, Graziadei A, Forbrig C, Bremenkamp R, Charles K, Lenz S, Elfmann C, Fischer L, Stülke J, Rappsilber J. Protein complexes in cells by AI-assisted structural proteomics. *Mol Syst Biol*. 2023 Apr 12;19(4):e11544.
147. Prindle JR, de Cuba OIC, Gahlmann A. Single-molecule tracking to determine the abundances and stoichiometries of freely-diffusing protein complexes in living cells: Past applications and future prospects. *J Chem Phys*. 2023 Aug 21;159(7):071002.
148. Manipur I, Giordano M, Piccirillo M, Parashuraman S, Maddalena L. Community Detection in Protein-Protein Interaction Networks and Applications. *IEEE/ACM Trans Comput Biol Bioinform*. 2023 Jan-Feb;20(1):217-237.
149. Wang YY, Li W, Ye BC, Bi XB. Chemical and Biological Strategies for Profiling Protein-Protein Interactions in Living Cells. *Chem Asian J*. 2023 Jul 17;18(14):e202300226.
150. Tatulian SA. Challenges and hopes for Alzheimer's disease. *Drug Discov Today*. 2022 Apr;27(4):1027-1043.
151. Karkisaval AG, Hassan R, Nguyen A, Balster B, Abedin F, Lal R, Tatulian SA. The structure of tyrosine-10 favors ionic conductance of Alzheimer's disease-associated full-length amyloid- $\beta$  channels. *Nat Commun*. 2024 Feb 13;15(1):1296.
152. Jackson M, Mantsch HH. The use and misuse of FTIR spectroscopy in the determination of protein structure. *Crit Rev Biochem Mol Biol*. 1995;30(2):95-120.
153. Cline EN, Bicca MA, Viola KL, Klein WL. The Amyloid- $\beta$  Oligomer Hypothesis: Beginning of the Third Decade. *J Alzheimers Dis*. 64(s1), S567–S610 (2018).
154. Li S, Selkoe DJ. A mechanistic hypothesis for the impairment of synaptic plasticity by soluble A $\beta$  oligomers from Alzheimer's brain. *J Neurochem*. 2020 Sep;154(6):583-597.



155. Khaled M, Rönnbäck I, Ilag LL, Gräslund A, Strodel B, Österlund N. A Hairpin Motif in the Amyloid- $\beta$  Peptide Is Important for Formation of Disease-Related Oligomers. *J Am Chem Soc.* 2023 Aug 23;145(33):18340-18354.
156. Ravens U, Dobrev D. Regulation of sarcoplasmic reticulum Ca(2+)-ATPase and phospholamban in the failing and nonfailing heart. *Cardiovasc Res.* 2000 Jan 1;45(1):245-52.
157. Tatulian SA, Chen B, Li J, Negash S, Middaugh CR, Bigelow DJ, Squier TC. The inhibitory action of phospholamban involves stabilization of alpha-helices within the Ca-ATPase. *Biochemistry.* 2002 Jan 22;41(3):741-51.
158. Gustavsson M, Verardi R, Mullen DG, Mote KR, Traaseth NJ, Gopinath T, Veglia G. Allosteric regulation of SERCA by phosphorylation-mediated conformational shift of phospholamban. *Proc Natl Acad Sci USA* 110: 17338–17343, 2013.
159. Arnold ME, Dostmann WR, Martin J, Previs MJ, Palmer B, LeWinter M, Meyer M. SERCA2a-phospholamban interaction monitored by an interposed circularly permuted green fluorescent protein. *Am J Physiol Heart Circ Physiol.* 2021 Jun 1;320(6):H2188-H2200.
160. Morita T, Hussain D, Asahi M, Tsuda T, Kurzydowski K, Toyoshima C, MacLennan DH. Interaction sites among phospholamban, sarcolipin, and the sarco(endo)plasmic reticulum Ca(2+)-ATPase. *Biochem Biophys Res Commun.* 2008 Apr 25;369(1):188-94.
161. Tatulian SA, Jones LR, Reddy LG, Stokes DL, Tamm LK. Secondary structure and orientation of phospholamban reconstituted in supported bilayers from polarized attenuated total reflection FTIR spectroscopy. *Biochemistry.* 1995 Apr 4;34(13):4448-56.
162. Ihalainen JA, Paoli B, Muff S, Backus EH, Bredenbeck J, Woolley GA, Caflisch A, Hamm P. Alpha-Helix folding in the presence of structural constraints. *Proc Natl Acad Sci U S A.* 2008 Jul 15;105(28):9588-93.
163. Manor J, Arbely E, Beerlink A, Akkawi M, Arkin IT. Use of Isotope-Edited FTIR to Derive a Backbone Structure of a Transmembrane Protein. *J Phys Chem Lett.* 2014 Aug 7;5(15):2573-9.
164. Dhayalan B, Fitzpatrick A, Mandal K, Whittaker J, Weiss MA, Tokmakoff A, Kent SB. Efficient Total Chemical Synthesis of (13) C=(18) O Isotopomers of Human Insulin for Isotope-Edited FTIR. *Chembiochem.* 2016 Mar 2;17(5):415-20.
165. Tang S, Zuo C, Huang DL, Cai XY, Zhang LH, Tian CL, Zheng JS, Liu L. Chemical synthesis of membrane proteins by the removable backbone modification method. *Nat Protoc.* 2017 Dec;12(12):2554-2569.
166. Davis CM, Cooper AK, Dyer RB. Fast helix formation in the B domain of protein A revealed by site-specific infrared probes. *Biochemistry.* 2015 Mar 10;54(9):1758-66.
167. Aisenbrey C, Cusan M, Lambotte S, Jasperse P, Georgescu J, Harzer U, Bechinger B. Specific isotope labeling of colicin E1 and B channel domains for membrane topological analysis by oriented solid-state NMR spectroscopy. *Chembiochem.* 2008 Apr 14;9(6):944-51.
168. Iwasaki T, Miyajima-Nakano Y, Fukazawa R, Lin MT, Matsushita SI, Hagiuda E, Taguchi AT, Dikanov SA, Oishi Y, Gennis RB. Escherichia coli amino acid auxotrophic expression host strains for investigating protein structure-function relationships. *J Biochem.* 2021 Apr 29;169(4):387-394.
169. Saebi A, Brown JS, Marando VM, Hartrampf N, Chumbler NM, Hanna S, Poskus M, Loas A, Kiessling LL, Hung DT, Pentelute BL. Rapid Single-Shot Synthesis of the 214 Amino



- Acid-Long N-Terminal Domain of Pyocin S2. *ACS Chem Biol.* 2023 Mar 17;18(3):518-527.
170. Sato K, Farquhar CE, Rodriguez J, Pentelute BL. Automated Fast-Flow Synthesis of Chromosome 9 Open Reading Frame 72 Dipeptide Repeat Proteins. *J Am Chem Soc.* 2023 Jun 21;145(24):12992-12997.
171. Zhang TO, Grechko M, Moran SD, Zanni MT. Isotope-Labeled Amyloids via Synthesis, Expression, and Chemical Ligation for Use in FTIR, 2D IR, and NMR Studies. *Methods Mol Biol.* 2016;1345:21-41.
172. Zheng JS, He Y, Zuo C, Cai XY, Tang S, Wang ZA, Zhang LH, Tian CL, Liu L. Robust Chemical Synthesis of Membrane Proteins through a General Method of Removable Backbone Modification. *J Am Chem Soc.* 2016 Mar 16;138(10):3553-61.
173. Gan SW, Surya W, Vararattanavech A, Torres J. Two different conformations in hepatitis C virus p7 protein account for proton transport and dye release. *PLoS One.* 2014 Jan 7;9(1):e78494.
174. Vandersteen A, Masman MF, De Baets G, Jonckheere W, van der Werf K, Marrink SJ, Rozenski J, Benilova I, De Strooper B, Subramaniam V, Schymkowitz J, Rousseau F, Broersen K. Molecular plasticity regulates oligomerization and cytotoxicity of the multi-peptide-length amyloid- $\beta$  peptide pool. *J Biol Chem.* 2012 Oct 26;287(44):36732-43.
175. Abedin F, Kandel N, Tatulian SA. Effects of A $\beta$ -derived peptide fragments on fibrillogenesis of A $\beta$ . *Sci Rep.* 2021 Sep 28;11(1):19262.
176. Matos JO, Goldblatt G, Jeon J, Chen B, Tatulian SA. Pyroglutamylated amyloid- $\beta$  peptide reverses cross  $\beta$ -sheets by a prion-like mechanism. *J Phys Chem B.* 2014 May 29;118(21):5637-43.
177. Xu Y, Filice CT, Leonenko Z. Protective effect of trehalose sugar on amyloid-membrane interactions using BLM electrophysiology. *Biophys J.* 2024 May 15:S0006-3495(24)00326-6.
178. Abedin F, Tatulian SA. Mutual structural effects of unmodified and pyroglutamylated amyloid  $\beta$  peptides during aggregation. *J Pept Sci.* 2021 Jun;27(6):e3312.
179. Kimura Y, Imanishi M, Li Y, Yura Y, Ohno T, Saga Y, Madigan MT, Wang-Otomo ZY. Identification of metal-sensitive structural changes in the Ca<sup>2+</sup>-binding photocomplex from *Thermochromatium tepidum* by isotope-edited vibrational spectroscopy. *J Chem Phys.* 2022 Mar 14;156(10):105101.
180. Tatulian SA, Biltonen RL, Tamm LK. Structural changes in a secretory phospholipase A2 induced by membrane binding: a clue to interfacial activation? *J Mol Biol.* 1997 May 23;268(5):809-15.
181. Flach CR, Cai P, Dieudonné D, Brauner JW, Keough KM, Stewart J, Mendelsohn R. Location of structural transitions in an isotopically labeled lung surfactant SP-B peptide by IRRAS. *Biophys J.* 2003 Jul;85(1):340-9.
182. Waeytens J, Van Hemelryck V, Deniset-Besseau A, Ruyschaert JM, Dazzi A, Raussens V. Characterization by Nano-Infrared Spectroscopy of Individual Aggregated Species of Amyloid Proteins. *Molecules.* 2020 Jun 24;25(12):2899.
183. Banerjee S, Naik T, Baghel D, Ghosh A. Intermediate Antiparallel Fibrils in A $\beta$ 40 Dutch Mutant Aggregation: Insights from Nanoscale Infrared Spectroscopy. *J Phys Chem B.* 2023 Jul 6;127(26):5799-5807.



184. Dou T, Zhou L, Kurouski D. Unravelling the Structural Organization of Individual  $\alpha$ -Synuclein Oligomers Grown in the Presence of Phospholipids. *J Phys Chem Lett.* 2021 May 13;12(18):4407-4414.
185. Rodriguez A, Ali A, Holman AP, Dou T, Zhaliyazka K, Kurouski D. Nanoscale structural characterization of transthyretin aggregates formed at different time points of protein aggregation using atomic force microscopy-infrared spectroscopy. *Protein Sci.* 2023 Dec;32(12):e4838.
186. Ruggeri FS, Mannini B, Schmid R, Vendruscolo M, Knowles TPJ. Single molecule secondary structure determination of proteins through infrared absorption nanospectroscopy. *Nat Commun.* 2020 Jun 10;11(1):2945.
187. Pięta E. Nanoscale insight into biochemical changes in cervical cancer cells exposed to adaptogenic drug. *Micron.* 2023 Jul;170:103462.
188. Tatulian SA. Structural Dynamics of Insulin Receptor and Transmembrane Signaling. *Biochemistry.* 2015 Sep 15;54(36):5523-32.
189. Kinoshita-Kikuta E, Kinoshita E, Suga M, Higashida M, Yamane Y, Nakamura T, Koike T. Characterization of Phosphorylation Status and Kinase Activity of Src Family Kinases Expressed in Cell-Based and Cell-Free Protein Expression Systems. *Biomolecules.* 2021 Oct 2;11(10):1448.
190. Gurzeler LA, Ziegelmüller J, Mühlemann O, Karousis ED. Production of human translation-competent lysates using dual centrifugation. *RNA Biol.* 2022 Jan;19(1):78-88.
191. Anderson JC, Wu N, Santoro SW, Lakshman V, King DS, Schultz PG. An expanded genetic code with a functional quadruplet codon. *Proc Natl Acad Sci U S A.* 2004 May 18;101(20):7566-71.
192. Gao R, Zhang Y, Choudhury AK, Dedkova LM, Hecht SM. Analogues of vaccinia virus DNA topoisomerase I modified at the active site tyrosine. *J Am Chem Soc.* 2005 Mar 16;127(10):3321-31.
193. Xiao H, Chatterjee A, Choi SH, Bajjuri KM, Sinha SC, Schultz PG. Genetic incorporation of multiple unnatural amino acids into proteins in mammalian cells. *Angew Chem Int Ed Engl.* 2013 Dec 23;52(52):14080-3.
194. Osgood AO, Zheng Y, Roy SJS, Biris N, Hussain M, Loynd C, Jewel D, Italia JS, Chatterjee A. An Efficient Opal-Suppressor Tryptophanyl Pair Creates New Routes for Simultaneously Incorporating up to Three Distinct Noncanonical Amino Acids into Proteins in Mammalian Cells. *Angew Chem Int Ed Engl.* 2023 May 2;62(19):e202219269.
195. Peuker S, Andersson H, Gustavsson E, Maiti KS, Kania R, Karim A, Niebling S, Pedersen A, Erdelyi M, Westenhoff S. Efficient Isotope Editing of Proteins for Site-Directed Vibrational Spectroscopy. *J Am Chem Soc.* 2016 Feb 24;138(7):2312-8.
196. Goto Y, Katoh T, Suga H. Flexizymes for genetic code reprogramming. *Nat Protoc.* 2011 Jun;6(6):779-90.
197. Coronado JN, Ngo P, Anslyn EV, Ellington AD. Chemical insights into flexizyme-mediated tRNA acylation. *Cell Chem Biol.* 2022 Jul 21;29(7):1071-1112.
198. Zheng Y, Addy PS, Mukherjee R, Chatterjee A. Defining the current scope and limitations of dual noncanonical amino acid mutagenesis in mammalian cells. *Chem Sci.* 2017 Oct 1;8(10):7211-7217.
199. Meineke B, Heimgärtner J, Caridha R, Block MF, Kimler KJ, Pires MF, Landreh M, Elsässer SJ. Dual stop codon suppression in mammalian cells with genomically integrated genetic code expansion machinery. *Cell Rep Methods.* 2023 Nov 20;3(11):100626.





200. Sisido M, Ninomiya K, Ohtsuki T, Hohsaka T. Four-base codon/anticodon strategy and non-enzymatic aminoacylation for protein engineering with non-natural amino acids. *Methods*. 2005 Jul;36(3):270-8.
201. Dunkelmann DL, Oehm SB, Beattie AT, Chin JW. A 68-codon genetic code to incorporate four distinct non-canonical amino acids enabled by automated orthogonal mRNA design. *Nat Chem*. 2021 Nov;13(11):1110-1117.



## Data Availability

No primary research results, software or code have been included and no new data were generated or analyzed as part of this review.

